SANDIA REPORT
SAND2007-0399
Unlimited Release
Printed February 2007

3D Optical Sectioning with a New Hyperspectral Confocal Fluorescence Imaging System

David M. Haaland, Michael B. Sinclair, Howland D. T. Jones, Jerilyn A. Timlin, Linda T. Nieman, George D. Bachand, Darryl Y. Sasaki, George S. Davidson, and Mark H. Van Benthem

Prepared by
Sandia National Laboratories
Albuquerque, New Mexico 87185 and Livermore, California 94550

Sandia is a multiprogram laboratory operated by Sandia Corporation, a Lockheed Martin Company, for the United States Department of Energy's National Nuclear Security Administration under Contract DE-AC04-94AL85000.

Issued by Sandia National Laboratories, operated for the United States Department of Energy by Sandia Corporation.

Available to DOE and DOE contractors from
U.S. Department of Energy
Office of Scientific and Technical Information
P.O. Box 62
Oak Ridge, TN 37831

Telephone: (865) 576-8401
Facsimile: (865) 576-5728
E-Mail: reports@adonis.osti.gov
Online ordering: http://www.osti.gov/bridge

Available to the public from
U.S. Department of Commerce
National Technical Information Service
5285 Port Royal Rd.
Springfield, VA 22161

Telephone: (800) 553-6847
Facsimile: (703) 605-6900
E-Mail: orders@ntis.fedworld.gov
Online order: http://www.ntis.gov/help/ordermethods.asp?loc=7-4-0#online

SAND2007-0399
Unlimited Release
Printed February 2007

3D Optical Sectioning with a New Hyperspectral Confocal Fluorescence Imaging System

David M. Haaland, Biomolecular Analysis & Imaging
Michael B. Sinclair, Microsystem Materials
Howland D. T. Jones, Biomolecular Analysis & Imaging
Jerilyn A. Timlin, Biomolecular Analysis & Imaging
Linda T. Nieman, Biomolecular Analysis & Imaging
George D. Bachand, Biomolecular Interfaces & Systems
Darryl Y. Sasaki, Biomolecular Interfaces & Systems
George S. Davidson, Computation, Computers & Math
Mark H. Van Benthem, Biomolecular Analysis & Imaging

Sandia National Laboratories
P.O. Box 5800
Albuquerque, NM 87185-0895

Abstract

A novel hyperspectral fluorescence microscope for high-resolution 3D optical sectioning of cells and other structures has been designed, constructed, and used to investigate a number of different problems. We have significantly extended new multivariate curve resolution (MCR) data analysis methods to deconvolve the hyperspectral image data and to rapidly extract quantitative 3D concentration distribution maps of all emitting species. The imaging system has many advantages over current confocal imaging systems including simultaneous monitoring of numerous highly overlapped fluorophores, immunity to autofluorescence or impurity fluorescence, enhanced sensitivity, and dramatically improved accuracy, reliability, and dynamic range. Efficient data compression in the spectral dimension has allowed personal computers to perform quantitative analysis of hyperspectral images of large size without loss of image quality. We have also developed and tested software to perform analysis of time resolved hyperspectral images using trilinear multivariate analysis methods. The new imaging system is an enabling technology for numerous applications including 1) 3D composition mapping analysis of multicomponent processes occurring during host-pathogen interactions, 2) monitoring microfluidic processes, 3) imaging of molecular motors and 4) understanding photosynthetic processes in wild type and mutant *Synechocystis* cyanobacteria.

Acknowledgements

The authors would like to acknowledge the contributions of Professor Willem Vermaas and Sawsan Hamad of Arizona State University for preparation and interpretation of the *Synechocystis* cells and experiments. We would also like to thank David K. Melgaard, Christopher Stork, and Michael R. Keenan of Sandia National Laboratories for the software that they have developed that has been used in some of the analyses reported here.

Table of Contents

Introduction

Microscopy is a fundamental tool for biologists to image and understand living systems at the cellular and subcellular level. In particular, confocal, filter-based fluorescence microscopes have given biologists a tool to monitor processes in living cells at diffraction-limited spatial resolutions in three dimensions. However, this technology has numerous limitations such as 1) being limited to monitoring just a few fluorescent tags at a time, and 2) less than quantitative image quality due to cross-talk between overlapping fluorophores and sources of autofluorescence, and the lack of contrast for weak emission sources in the presence of autofluorescence. We have addressed these limitations with the development of a new hyperspectral microscope. At Sandia, a new 3-dimensional (3D) hyperspectral confocal fluorescence microscope has been designed, constructed, and is currently being used to obtain excellent quality hyperspectral images for many different applications. The microscope is able to collect an entire emission spectrum at each voxel in the image. The term hyperspectral simply refers to the fact that hundreds of wavelengths are collected at each voxel (512 wavelengths over the visible and near infrared region of the spectrum for the system described in this report). The new microscope system with associated software allows many fluorophores to be monitored simultaneously and quantitatively without concern for spectral crosstalk or interference from autofluorescence or unknown sources of emission. Software has been developed to operate the microscope, give immediate spectral details for selected voxels, and provide image information based upon simulating an optimal 3-color filter-based microscope. The operational characteristics of the microscope have been carefully determined including spatial resolution, noise characteristics and spectral response.

The new hyperspectral confocal fluorescence microscope along with the associated fast and rigorous multivariate curve resolution (MCR) software used to analyze the image data sets is unique and offers a new technology for biologists to study complex processes occurring in living cells. This new fluorescence microscope system (microscope and associated multivariate analysis software) allows much more quantitative information to be obtained from the confocal images than possible with current commercial microscopes when autofluorescence and multiple fluorophore labels are present in the cells. The use of the MCR software applied to the hyperspectral images allows all the pure spectra of the fluorescing species to be “discovered” directly from the image data and their relative concentrations to be accurately displayed in three dimensions without the need for any standards or *a priori* information. Significant improvements in the software for visualization of hyperspectral images and spectra has been completed, and multivariate curve resolution (MCR) software for extracting pure emission spectra and relative concentrations has continued to be upgraded with the formation of a new Graphical User Interface (GUI) program. This GUI-based software not only significantly improves the ease of operation of the software, but also makes it possible for non-experts to use the software.

Work has progressed in applications related to the imaging of motor proteins and the detailed investigation of lipid bilayers. We have used the microscope to also image live *Synechocystis* wild-type and mutant bacteria to quantitatively study the spatial distributions of the photosynthetic pigments in the bacteria in three dimensions. With this new technology, we have been able to accurately and quantitatively image the six spatially and spectrally overlapping photosynthetic pigments in Synechocystis wild-type and mutant cyanobacteria at diffraction-limited spatial resolutions (250 x 250 x 600 nanometers). These results show that hyperspectral fluorescence imaging can provide unique quantitative information regarding heterogeneity of pigment organization and localization in the cells even when there is high spectral and spatial overlap of the fluorescent pigments.

In **Section 1** of the report, we present a description of the multivariate curve resolution (MCR) algorithms used in the analysis of the hyperspectral images. The GUI-based hyperspectral MCR analysis software is then described with a few examples. In **Section 2**, we describe the new hyperspectral microscope design, operation, and relevant operating characteristics. We also present some simple imaging experiments that help to characterize and demonstrate the use of the new microscope. **Section 3** presents the initial implementation of three-dimensional deconvolution algorithms designed to improve the spatial resolution of the deconvolved images. **Section 4** describes work performed in the application areas of imaging live Synechocystis cells, supported lipid bilayers on glass microbeads, and three-dimensional assemblies of microtubules and fluorescently tagged kinesin motor proteins. In **Section 5**, we present the analysis of time-resolved hyperspectral images in a multivariate analysis method that takes advantage of the 3-way trilinear nature of the data to extract pure emission spectra, relative concentration maps, and decay curves for fluorophores within the images that are being photobleached.

Section 1. Multivariate Curve Resolution Algorithms and Software.

The initial part of this explanation is based upon the methods described previously.[1.1] The multivariate curve resolution (MCR) methods used in this work are based on constrained alternating least squares algorithms.[1.2] In all cases, rigorous least squares methods are used. The algorithms are based on classical least squares (CLS) calibration and prediction methods.[1.3, 1.4] In the following discussion, matrices are represented as bold uppercase letters, column vectors as bold lowercase letters, row vectors are represented as transposed column vectors, transposed matrices and vectors are denoted by a superscript T, and the pseudoinverse of a matrix is denoted by a superscript +. The CLS model for the fluorescence data assumes an additive linear model following the relationship,

$$\mathbf{D} = \mathbf{C}\mathbf{S}^{T} + \mathbf{E} \quad (1)$$

where **D** is the $n \times p$ matrix of n spectra each containing p intensities as a function of wavelength, **C** is the $n \times m$ matrix of component concentrations where m corresponds to the number of components, $\mathbf{S}^{T}$ is the $m \times p$ matrix of pure-component spectra, and **E** is the $n \times p$ matrix of spectral residuals.

Principal component analysis (PCA) is generally used to determine the number of pure spectral species present in the data.[1.5] Instead of the normal application of PCA, we often weight the data to accommodate the fact the noise in the fluorescence signal is dominated by counting or Poisson statistics. Poisson distributed noise has the characteristic that the variance of the noise is proportional to the signal. Optimal weighting of the data was implemented to make the noise distribution of the weighted data more nearly uniform. The optimal weighting is obtained by premultiplying the spectral data matrix by the inverse square root of the mean image and postmultiplying the data matrix by the inverse square root of the mean spectrum [1.6]. PCA is applied directly to the weighted data. After conclusion of the analysis, the final results are then scaled by the corresponding inverses of the weighting matrices to obtain the results in the units of the original data. Often a semi-log plot of the singular values of the weighted PCA as a function of component number results in a clear demarcation to specify the number of components to include in the MCR analysis. We have found that if the wrong number of components is chosen, realistic pure emission spectra are not obtained.

Once the number of pure emission spectra is chosen, we initiate the MCR algorithm with a guess for $\mathbf{S}^{T}$. Initial guesses for the pure spectra in $\mathbf{S}^{T}$ can be random numbers, positive portions of the principal component loading vectors, reasonable spectral shapes based upon known pure-component spectra, or pure-component spectra derived from previous MCR analysis of similar data. The CLS estimate for **C**, denoted $\hat{\mathbf{C}}$, is obtained from

$$\hat{\mathbf{C}} = \mathbf{D}(\mathbf{S}^{T})^{+} \quad (2)$$

Once $\hat{\mathbf{C}}$ has been obtained, the CLS estimate for $\mathbf{S}^T$ can be obtained from

$$\hat{\mathbf{S}}^T = \mathbf{C}^+\mathbf{D} \qquad (3)$$

However, there are infinite possible solutions to Eq. 2 and 3 due to rotational ambiguity of the solution. We can limit the range of possible solutions by employing constraints. Since the concentrations and pure-component spectra should be all nonnegative, we employ a nonnegative constrained alternating least squares algorithm similar to that presented by Bro.[1.2] Improvements in the efficiency of Bro's algorithms have been implemented to dramatically reduce computation times.[1.7] The solutions to Eq. 2 and 3 are solved iteratively until the sum of squared spectral residuals converges to a specified tolerance level or a maximum number of iterations have been achieved.

We also apply equality constraints when appropriate [1.8] to further limit the range of possible solutions to Eq. 2 and 3. The method of direct elimination is used when employing equality constraints in order to assure rigorous least squares solutions to the constrained problem.[1.8] Equality constraints can be applied when all or a portion of the pure-component spectrum and/or concentrations are known. They are also applied to compensate for a variable amount of offset signal and/or dark signal present in our CCD detector output. In addition, if some components are known to be absent from a region of the image, an equality constraint with zero concentration can be applied to those pixels for components that are known to be absent from the specified region of the spectrum.

Significant improvements to the software and the MCR algorithms were accomplished during the course of this project and with auxiliary funding from several different projects. For example, monotonic and unimodal constraints were added to the MCR analysis. Since pure fluorescence emission species often have unimodal character, the implementation of unimodal constraints can minimize the presences of mixing of pure spectra due to rotational ambiguities. In addition, monotonic constraints can be added to just the leading edge of a pure spectral emission component for those cases where the pure spectra might not be unimodal throughout the spectrum.

In addition, the C-coded MCR software (1.9) has been incorporated into a Matlab GUI-based software module that calls the fast MCR code. The GUI-based code was designed to greatly improve the efficiency of the MCR analysis, enhance reliability of the results, and make the software sufficiently user friendly that nonexperts will be able to use the software. The GUI-based software can read multiple hyperspectral data formats that are used at Sandia National Laboratories. It also makes selection of various MCR options, starting spectra, nonnegativity constraints, equality constraints, and unimodal and monotonic constraints quite straightforward. In addition, regions of interest can be selected based upon spectral intensities or concentration levels of selected components based upon a preliminary MCR analysis. The GUI-based MCR software also generates a variety of output plots to view and evaluate the quality of the MCR

analyses. Standard output plots include, semilog eigenvalue vs. number of eigenvectors vectors from the PCA analysis, PCA eigenvectors, pure emission spectra for all components, concentration image maps for each component, PCA analysis of the spectral residuals including residual eigenvectors and score image maps, percent variance described by each pure component and the percent variance described by each eigenvector of the spectral residuals, and finally, red-green-blue (RGB) images of user selected components. The results from each MCR analysis are stored in a report file that can be recalled for further plotting or initiation of similar but new MCR analyses. Our software possesses a great deal of flexibility when applying constraints to the alternating least squares algorithm. This allows us to use all of the spectral and spatial information known about a data cube and thus minimizes the rotational ambiguity in order to converge to the most realistic solution. The software now works with full 3D spectral image data or time-resolved 2D spectral image data. Any or all individual z sections or time slices in the data set can be selected for analysis or display.

Figure 1.1 shows a screen shot of the GUI-based MCR software with typical parameters selected. Figure 1.2 illustrates a screen shot of some of the standard plots that are automatically generated after performing an MCR analysis of the hyperspectral image data.

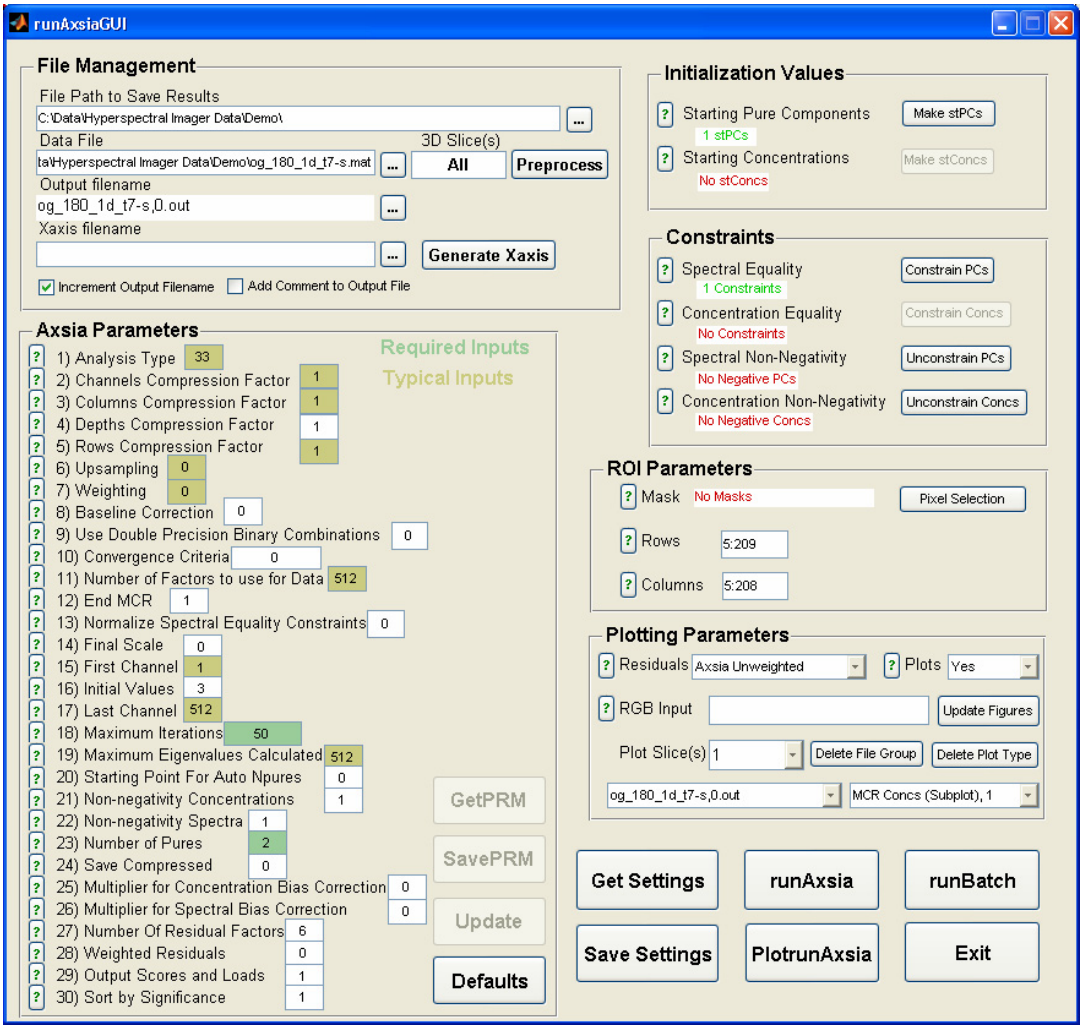

Figure 1.1 Screen shot of the GUI-based MCR software with typical parameters selected.

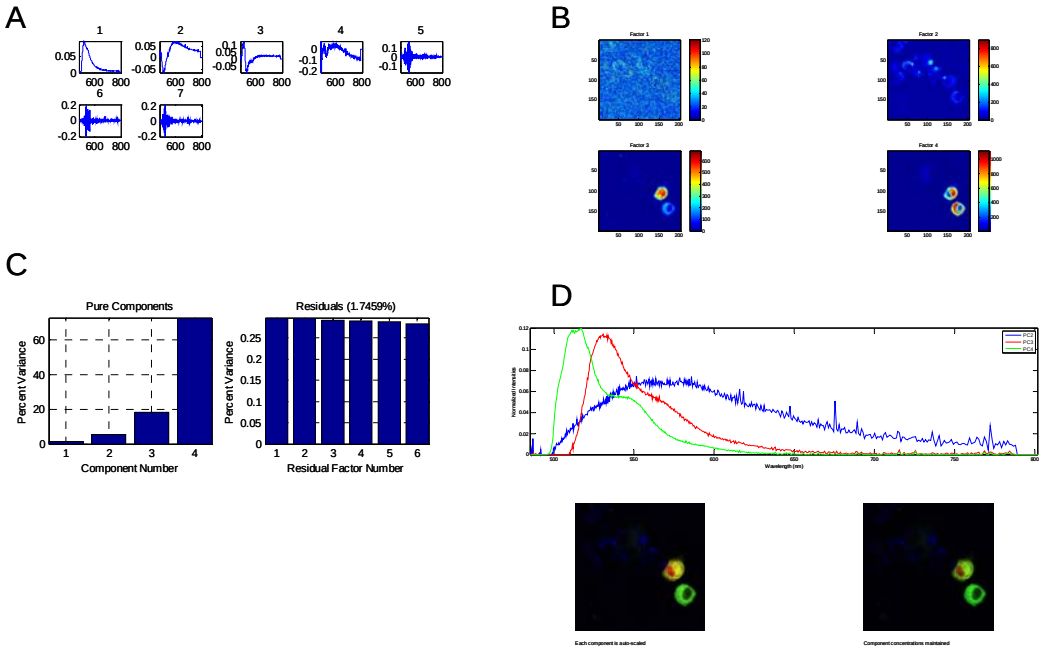

Figure 1.2. Screen shot of some of the standard plots that are automatically generated after performing an MCR analysis of the hyperspectral image data. A) First 7 principle component loading vectors from the spectra in the image, B) Concentration maps for the pure components in the image, C) Percent variances accounted for by the pure components and the PCA loading vectors of the spectral residuals, D) Pure component emission spectra and RGB images of the concentration maps.

Section 1 References

1.1 Davidson, G. S., D. M. Haaland, S. Martin, J. A. Timlin, M. B. Sinclair, M. H. Van Benthem, M. R. Keenan, E. V. Thomas, K. W. Boyack, B. N. Wylie, J. Cowie, J. Martinez, A. Aragon, M. Werner-Washburne, M. Mosquera-Caro, and C. Willman, *High Throughput Instruments, Methods, and Informatics for Systems Biology*, SAND2003-4664, December 2003.

1.2 Bro, R. and S. DeJong, *A fast non-negativity-constrained least squares algorithm*. In *Journal of Chemometrics*. Vol. 11. 1997. 393-401.

1.3 Haaland, D. M., R. G. Easterling, and D. A. Vopicka, *Multivariate Least-Squares Methods Applied to the Quantitative Spectral-Analysis of Multicomponent Samples*, in *Applied Spectroscopy*. 1985. p. 73-83.

1.4. Haaland, D. M. *Multivariate calibration methods applied to quantitative FT-IR analyses*. in *Practical Fourier Transform Infrared Spectroscopy*. 1990. San Diego: Academic Press.

1.5. Jolliffe, I. T., *Principal Component Analysis*. 1986, Springer-Verlag: New York.

1.6. Keenan, M. R. and P. G. Kotula, *Accounting for Poisson noise in the multivariate analysis of ToF-SIMS spectrum images*, *Surf. Interface Anal.* **36**, 2004, p. 203–212.

1.7 Van Benthem, M. H. and M. R. Keenan, *Fast algorithm for the solution of large-scale non-negativity-constrained least squares problems*, in *Journal of Chemometrics* **18**, 2004, p. 441-450.

1.8. Van Benthem, M. H., M. R. Keenan, and D. M. Haaland, *Application of equality constraints on variable during alternating least squares procedures*, in *Journal of Chemometrics*. 2002. p. 613-622.

1.9 Kotula, P. G., M. R. Keenan, and J. R. Michael, *Automated Analysis of SEM X-Ray Spectral Images: A Powerful New Microanalysis Tool*, in *Microsc. Microanal.* **9**, 2003, p. 1–17.

Section 2. Hyperspectral Microscope Design

A schematic diagram of the microscope layout is shown in Figure 2.1. The laser excitation source is a solid state 488 nm laser (Coherent Inc.). The output of the laser is attenuated and then spatially filtered to expand the beam and improve the mode quality. The laser light is then reflected from a dichroic filter (Chroma Inc.) and directed onto a galvanometer-driven mirror (Cambridge Technologies). As described below, the oscillations of the galvo-mirror cause the focused laser light to scan in the y-direction. An afocal telescope comprising an f = 125 mm achromatic doublet (Newport Corporation) and an f = 200 mm tube lens (Nikon) is used to further expand the laser beam in order to fill the back aperture of the objectives employed. The optical design and placement of this telescope are chosen to ensure that galvanometer driven mirror and the objective aperture lie in conjugate planes. Next, the excitation beam is directed onto the back aperture of the objective by means of a spectrally neutral beamsplitter (80% reflective, 20% transmissive). The laser light is then focused into the specimen using either a 20X, NA 0.75 Plan Apochromat objective (Nikon), or an oil immersion 60X, NA 1.4 Plan Apochromat (Nikon). In addition, a 100X LCD inspection objective (Nikon), optimized for imaging through thicker cover glass, can be used.

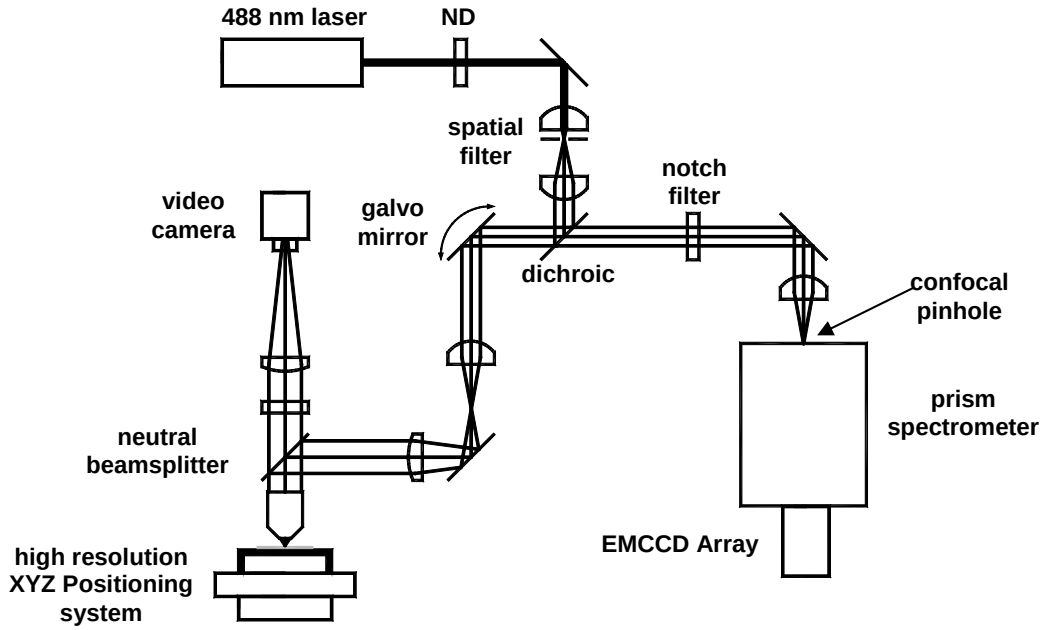

Figure 2.1. A schematic diagram of the layout of the hyperspectral confocal microscope.

A high power light emitting diode (Nichia) is mounted below the specimen as an illumination source for wide-field, transmitted light imaging of the specimen. Light from this source traverses the specimen and is collected by the objective. A portion (20%) of the collected light passes through the neutral beamsplitter and is focused by a tube lens onto a CCD video camera (Sony). The video output from the camera is recorded by a frame grabber (National Instruments) installed in the system computer.

The specimen is mounted on a piezoelectrically driven z-axis stage (Physik Istrumente) which, in turn, is mounted on a high precision (20 nm resolution), linear-motor driven XY translation stage (Aerotech). The fluorescent photons generated within the excitation volume are collected by the objective, propagate back through the optical path, and are descanned by the galvo-mirror. After passing through the dichroic filter the fluorescent emission is directed through a rugate notch filter (Edmund Industrial Optics) which further rejects scattered laser light. Finally, the fluorescent emission is focused by means of an f=200 mm achromatic doublet (Newport Corp.) onto a 50 µm diameter pinhole which also serves as the entrance aperture of the prism spectrometer. The fluorescent light is dispersed by the prism spectrometer and detected by a backside thinned EMCCD array (Andor Technologies). This detector's on-chip electron multiplication allows the charge from a single photoelectron to be amplified in excess of the read noise and thereby allows extremely sensitive detection at high readout rates (10 MHz).[2.1] In addition, backside thinning results in high quantum efficiency (~0.8).

The optical layout of the custom fabricated prism spectrometer is shown in Figure 2.2. The design of this spectrometer is based upon the aplanatic principles described in Reference 2.12. Light enters the spectrometer through the entrance slit and is directed through an aplanatic prism fabricated from Schott SF11 glass. Both surfaces of the prism are spherical, but are oriented relative to each other with a significant wedge angle.[2.2] A spherical mirror reflects the light back through the prism, and a dispersed image of the slit is formed at the plane of the detector. This spectrometer was designed to also be used as an imaging spectrometer in a hyperspectral microarray scanner [2.3] and exhibits near diffraction limited performance from 490 nm to 800 nm, and across a 10 mm tall entrance slit. In the current application, the entrance slit is replaced by a pinhole (the confocal pinhole) and the spectrometer is used on-axis vertically. Importantly, both surfaces of the aplanatic prism are coated with broadband antireflection coatings to maximize optical throughput.

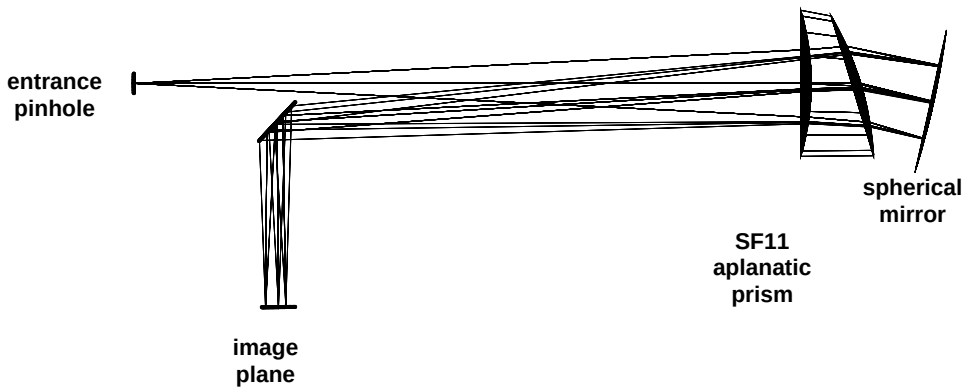

Figure 2.2: An optical raytrace of the aplanatic prism spectrometer

Confocal images are obtained through a combination of laser scanning and stage scanning (see Figure 2.3). A computer generated voltage waveform is used to repeatedly scan the angle of the galvanometer-driven mirror. This causes the focused laser spot to move with constant speed in the y-direction within the specimen. When the galvo-mirror reaches the end of a trace it is rapidly re-positioned to start the next trace. The XY stage on which the specimen is mounted moves at constant velocity in the x-direction. Thus, subsequent y-scans occur at increasing x-locations and a two-dimensional image is recorded. The Z-stage can then be moved to allow the acquisition of further two-dimensional images from planes deeper within the specimen.

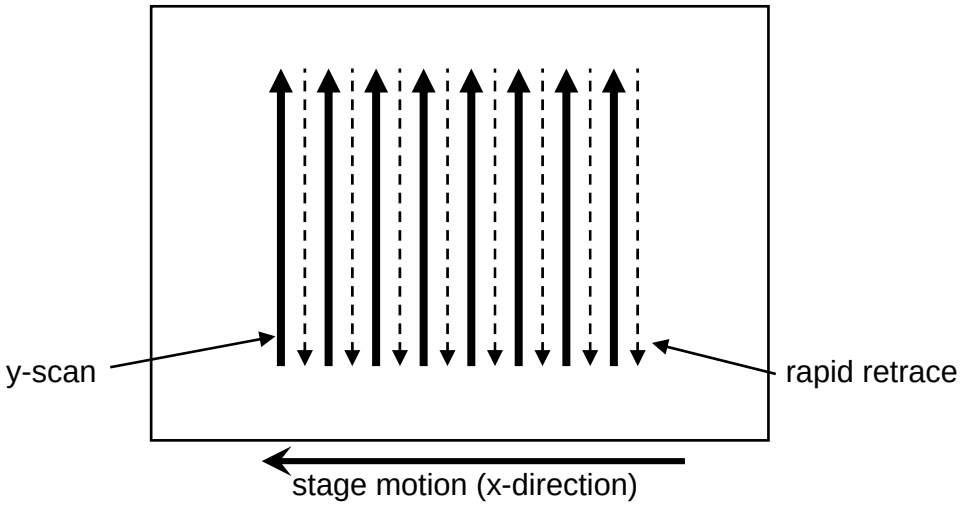

Figure 2.3. A diagram showing the scan geometry for the hyperspectral confocal microscope. A galvanometer driven mirror scans the focused laser spot in the y-direction, while a translation stage moves the specimen in the x-direction.

During each of the galvo-mirror traces, a second computer generated voltage waveform triggers the readout of the EMCCD detector at small increments along the trace. For example, the total length of a trace in the y-direction might be 25 μm, with the detector readout being triggered with 0.12 μm increments. A schematic of the EMCCD readout mode [2.4, 2.5] is shown in Figure 2.4. The pinhole diameter of 50 μm corresponds to approximately three pixels of the EMCCD detector. The dispersed image of the confocal pinhole is projected on the CCD array, centered on the 4th row of pixels above the frame transfer region. Each time the CCD receives an external trigger pulse, it shifts the photogenerated charge down by 8 rows. A new exposure interval begins, and with the next trigger the results for both exposure intervals are shifted down by another 8 rows. Thus, the photocharge produced during one exposure interval is shifted down with successive triggers until it is finally shifted into the serial register and digitized. Using this approach, the EMCCD detector can acquire 14-bit data at a sustained readout rate of 8.3 MB/s, corresponding to 8,300 spectra per second, with 512 points per spectrum. The speed of data acquisition is not compromised through the use of this readout mode: data rate achieved here is comparable to the rate that would be achieved if the detector were utilized in the fastest frame-transfer mode. In essence, this readout mode allows the two-dimensional EMCCD detector to behave as a fast readout, high quantum efficiency, 512 element linear diode array with single photon sensitivity. Such detectors are currently unavailable.

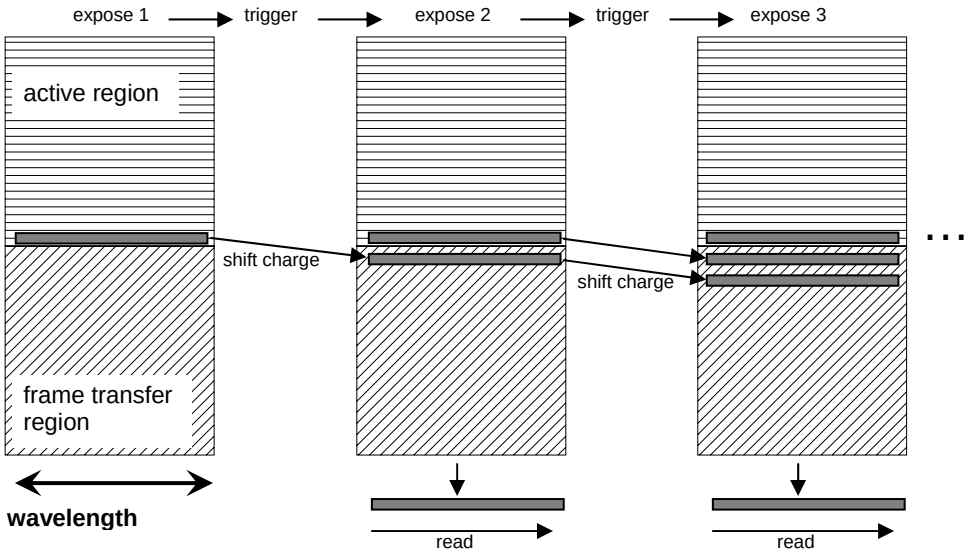

Figure 2.4. A schematic illustration of the EMCCD readout mode developed for the hyperspectral confocal microscope. The EMCCD array is illuminated within a small vertical range immediately adjacent to the frame transfer region of the detector. The photocharge generated during a given exposure interval is sequentially shifted down with successive trigger pulses until it is shifted into the serial register for readout.

A distinct advantage of this readout mode is the elimination of spectral artifacts, such as curvature [2.6] and keystone [2.7] that often plague spectral line imaging systems. In a traditional imaging spectrometer, the image of the straight entrance slit, projected on the detector, becomes slightly curved due to distortions induced by the spectrometer optics. In addition, the amount of curvature often varies with the wavelength. As a result of these distortions, correction algorithms must be applied to the raw data before further analysis can be performed.[2.6] In the present case, the spectrometer is not performing an imaging function. It is always used on axis, with the same few rows of the EMCCD exposed for each spatial location on the specimen. Hence no curvature or keystone distortions occur in the raw data.

The operation of the microscope is controlled by a personal computer. The computer contains I/O boards for the XY stage, the EMCCD detector, and the frame grabber. In addition, the computer houses a data acquisition card (National Instruments) that is used to produce the voltage waveforms that drive the galvo-mirror and trigger the EMCCD readout. An extensive control application, written in C++, coordinates the activities of each of these devices.

Microscope Performance

Because the confocal pinhole is employed in the traditional fashion, the spatial resolution of the hyperspectral confocal microscope is expected to be similar to the performance of conventional confocal microscopes. The 50 μm diameter of the confocal pinhole is slightly larger than the 41 μm diameter of the (magnified) Airy disk obtained with the 60X, NA 1.4 objective. This choice represents a compromise between the high optical throughput obtained with a large pinhole diameter and the improved spatial resolution and depth discrimination obtained with a small pinhole.[2.8, 2.9] The spatial resolution is expected to vary slightly as the emission wavelength varies from 500 nm to 800 nm. Post acquisition refinement of the spatial resolution of hyperspectral image stacks using deconvolution techniques will require the inclusion of a wavelength dependent detection point spread function. Note also that the confocal pinhole serves as the entrance aperture to the prism spectrometer and must remain relatively small to preserve good spectral resolution.

Figure 2.5a shows a small portion of one XY frame from a hyperspectral image stack obtained with a specimen containing 0.17 μm diameter fluorescent microspheres.[2.10] This image stack was acquired using the 60X, NA 1.4 objective. The x and y sampling intervals are 0.12 μm, and sequential frames were acquired with a z-spacing of 0.25 μm. The laser power at the sample was approximately 20 μW, and the exposure time was 240 μs per voxel. The emission spectrum recorded for the brightest pixel in this frame is shown in Fig. 2.5b. Figure 2.5c shows the intensity profile obtained from a linescan in the x-direction through the center of the sphere for the best focus frame. Both the full width at half maximum (FWHM) and the radius of the intensity profile are approximately 0.25 μm. For comparison, the expected lateral extent of the Airy disk in the object plane is 0.21 μm. A more precise determination of the lateral resolution would require measurement of significantly smaller spheres, or deconvolution to remove effects due to the finite width of the spheres utilized. Figure 2.5d shows an intensity profile corresponding to a line scan through the center of the sphere in the z-direction (i.e. the axial direction). In this case a FWHM of 0.6 μm is observed.

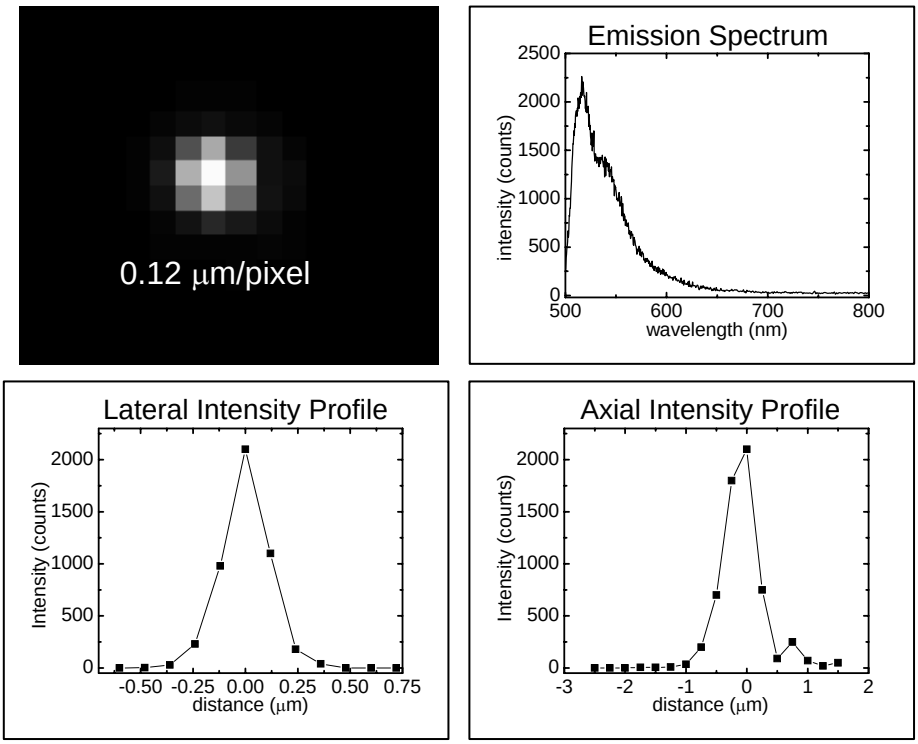

Figure 2.5. a) A small portion of a hyperspectral image stack, containing the image of a 0.17 μm diameter fluorescent microsphere. The pixels of this image were recorded at 0.12 μm intervals in the x- and y-directions. b) The emission spectrum of the microsphere, as recorded in the brightest pixel in the hyperspectral data set. c) A lateral intensity profile through the center of the microsphere, obtained from the in focus frame of the 3-dimensional image stack. d) An axial intensity profile through the center of the microsphere, obtained from successive frames of the 3-dimensional image stack.

To demonstrate the optical sectioning capability of the new microscope, a hyperspectral image stack was obtained with a specimen containing 2.5 μm diameter fluorescent microspheres.[2.11] The 60X, NA 1.4 objective was used for this measurement, and the x and y sampling intervals were 1.2 μm. Once again, the laser power was approximately 20 μW, and the exposure time was 240 μs per voxel. Figure 2.6a shows a sequence of ten x-y frames obtained with a z spacing of 0.3 μm between frames. Excellent optical sectioning is observed, consistent with the expectation that the spatial resolution of the hyperspectral microscope is comparable to that of conventional confocal microscopes. The gray scale images displayed in Figure 2.6a were obtained from the hyperspectral data by simply calculating the average intensity in the spectral range from 540 nm to 600 nm for each voxel. However, it must be emphasized that the full hyperspectral data set contains the entire emission spectrum for each voxel. A single voxel emission spectrum from one of the brighter voxels in this sequence is shown in Figure 2.6b. The entire hyperspectral data set corresponding to the

images shown in Figure 2.6a requires 100 MB of data storage. The results shown in Figs. 2.5 and 2.6 show that, as expected, the spatial resolution of the hyperspectral confocal microscope is comparable to that of traditional filter-based confocal systems.

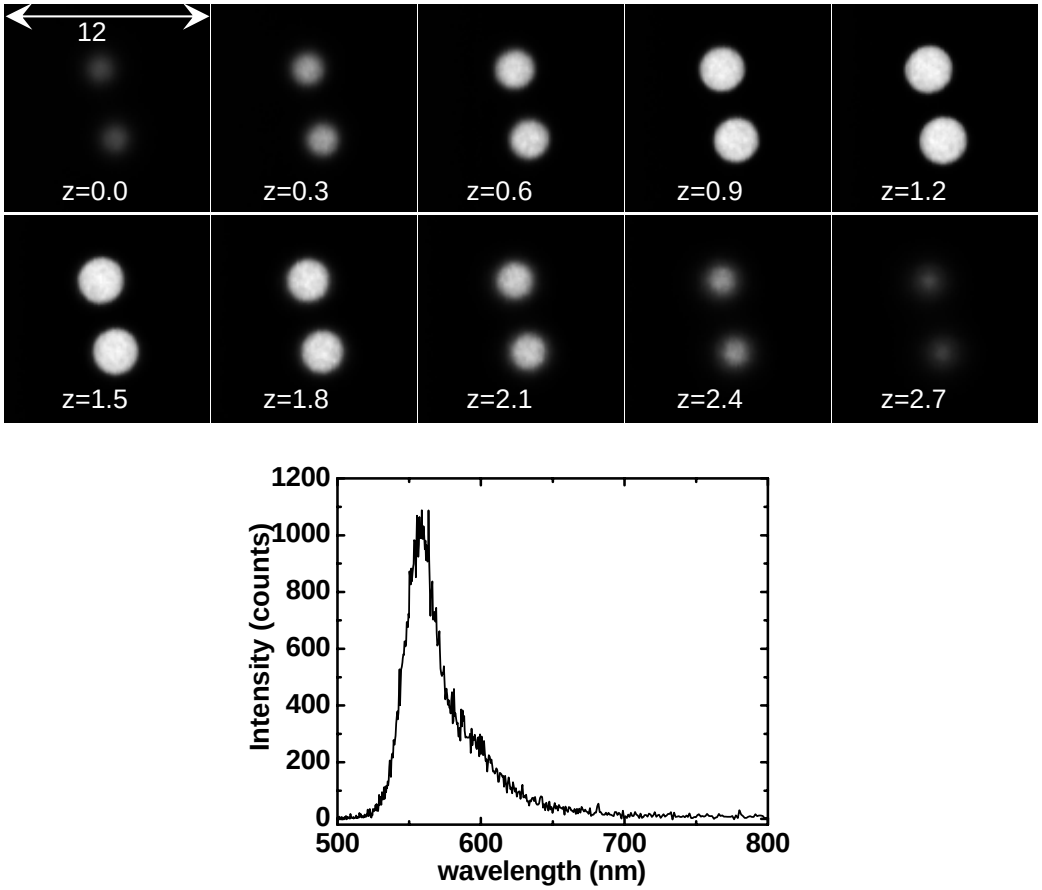

Figure 2.6. a) A sequence of gray scale images derived from a hyperspectral image stack obtained using 2.5 μm diameter fluorescent microspheres. The frames were recorded with 0.3 μm increments in the axial direction and show the optical sectioning performance of the hyperspectral confocal microscope. b) A single pixel emission spectrum corresponding to one of the brighter pixel of the hyperspectral data set.

Analysis of the hyperspectral data using multivariate techniques also enables the recovery of extremely weak spectral signatures. At first glance, one might expect that the hyperspectral approach of spreading a given number of photons across multiple detection channels would drastically reduce the signal-to-noise ratio (SNR) as compared to the traditional approach in which all the photons are detected within a single channel. In fact, this is true if only a single spectral bin of the hyperspectral data is used for the signal-to-noise determination. If all the

spectral channels are considered, and if read noise can be neglected (see below), the sensitivity of the hyperspectral approach is equivalent to that of a single channel instrument. As a simple example, consider a hypothetical emitter with a spectrum containing equal amplitudes in 10 contiguous spectral channels. If, on average, 100 photons are detected in each spectral channel, the SNR for a single spectral channel will be 10 (assuming Poisson statistics). In contrast, if all the available photons are detected in a single channel, as is the case with a traditional filter based instrument, a SNR of $\sqrt{1000}$ will be obtained. However, if the shape of the spectrum is known *a-priori*, simple signal averaging over the 10 spectral channels will result in a SNR of $\sqrt{1000}$, precisely the SNR that would be obtained with a single channel instrument. This conclusion holds true in the case of arbitrary spectral shapes, provided they are known in advance. Note that this discussion does not include the sensitivity enhancements of the hyperspectral data that are derived from the higher quantum efficiency of the backside thinned CCD array relative to that of a typical PMT photocathode.

In many important cases the spectra of the emitting species are not known in advance, and must be "discovered" from the hyperspectral data set. To do so, modern multivariate algorithms simultaneously considers all spectral channels for every pixel in the image. As a result, a significant amount of "signal averaging" occurs and the pure-component spectra can be determined with high signal-to-noise ratios even in the case where no single pixel contains high signal-to-noise ratio data.[2.12, 2.13] The low-noise pure-component spectra determined by the multivariate analysis can then be used as a basis for determining the concentration of each of the emitting species for every pixel of the image.

The role of detector read noise remains to be investigated. The on-chip amplification of the EMCCD detector amplifies the charge associated with a single photoelectron to a magnitude that exceeds the read noise, so that read noise can largely be neglected. However, some contribution of this noise is expected to remain and diminish the overall system sensitivity relative to a single channel instrument. Investigations are currently underway utilizing calibration samples to assess the impact of the detector read noise on the system performance.

Image acquisition is slower with the hyperspectral confocal microscope as compared to a traditional confocal microscope. Currently, the minimum dwell time per pixel (120 μs) is limited by the readout of the EMCCD detector. It is anticipated that further improvements in speed can be achieved through the development of faster readout electronics. In addition, the number of spectral channels recorded per pixel can be reduced somewhat without sacrificing spectral resolution. In contrast, conventional confocal microscopes can easily acquire images with dwell times of 20 μs or shorter. In fact, video rate instruments are available with dwell times in the ~100 ns range. The difference in speed between the hyperspectral and conventional microscopes is not surprising in view of the fact that the hyperspectral microscope acquires ~500

times more data per image pixel. However, in cases such as the *Synechocystis* results presented in **Section 4**, hyperspectral confocal microscopy represents the only approach for obtaining quantitative, high-resolution concentration maps for multiple spectrally and spatially overlapping species.

To carry out a more demanding test of the microscope's performance, a specimen was prepared that consisted of 2.3 μm silica microspheres suspended in poly(dimethylsiloxane) (PDMS) polymer. The surfaces of the silica microspheres were coated with biotin, which was then coupled to fluorescently labeled streptavidin.[2.14] Five different labels were employed: Oregon Green, R-Phycoerythrin, Alexa Fluor 610-R-PE, Alexa Fluor 647-R-PE, and Alexa Fluor 680-R-PE. Each microsphere was labeled with only a single type of fluorophore. All five types of microspheres were mixed and suspended in a ~30 μm thick PDMS polymer to endow the specimen with three-dimensional character. A 2-dimensional hyperspectral confocal image of this specimen is shown in Figure 4.1 in **Section 4**. This image was acquired using the 20X, NA 0.75 objective. The laser power was ~ 100 μW, and the exposure time was 240 μs per voxel. The data shown in this figure provide a demonstration of the ability of hyperspectral fluorescence microscopy to utilize multiple labels. In this case, *five different fluorescent tags were successfully imaged in a single scan*.

Since the microspheres are relatively well separated spatially, it is easy to find pixels that contain the emission spectrum of a single tag. In this case, the use of sophisticated multivariate analysis techniques is not essential. However, such an analysis can be performed [2.15] to determine the relative contributions of different fluorophores in regions where the beads overlap spatially. Interestingly, three of the labels utilized rely on fluorescence resonance energy transfer (FRET) between closely coupled Phycoerythrin donors and Alexa acceptors. For these labels, the use of multivariate analysis also allows for separation of the residual Phycoerythrin emission from the Alexa emissions.[2.16]

Section 2 References

2.1. C. D. Mackay, J. E. Baldwin, and R. N. Tubbs, “Noise free detectors in the visible and infrared: Implications for the design of next-generation AO systems and large telescopes”, in Future Giant Telescopes, J. R. P. Angel and R. Gilmozzi eds, Proc. SPIE **4840**; 436–442 (2003).

2.2. D. W. Warren, J. A. Hackwell and D. J. Gutierrez, “Compact prism spectrograph based on aplanatic principles”, Opt. Eng. **36**, 1174–82 (1997).

2.3. M. B. Sinclair, J. A. Timlin, D. M. Haaland, M. Werner-Washburne, “Design, construction, characterization, and application of a hyperspectral microarray scanner”, App. Opt. **43**, 2079–2088 (2004).

2.4. The EMCCD readout mode was developed and supplied by M. Catney of Andor Technologies.

2.5. P. Hing and H. W. Müller, “CCD Cameras Simplify Biological Analysis” Biophotonics, Sept. 2003, 52–58, (2003).

2.6. I. Pelletier, C. Pellerin, D. B. Chase, and J. F. Rabolt, “New developments in planar array infrared spectroscopy”, Appl. Spec. **59**, 156–163 (2005).

2.7. R. A. Neville, L. X. Sun; and K Staenz, “Detection of keystone in imaging spectrometer data”, in Algorithms and Technologies for MultiSpectral, Hyperspectral, and Ultraspectral Imagery X, S. S. Shen and P. E. Lewis eds., Proc. SPIE **5425** 208–217 (2004).

2.8. D. R. Sandison, R. M. Williams, K. S. Wells, J. Strickler, and W. W. Webb, “Quantitative Fluorescence Confocal Laser Scanning Microscopy (CLSM)”, in*, Handbook of Biological Confocal Microscopy 2nd Ed.*, J.B. Pauley, ed. (Plenum, New York, 1995) pp. 39–53.

2.9. R. H. Webb, “Confocal optical microscopy,” Rep. Prog. Phys. **59**, 427–471 (1996).

2.10. Invitrogen Corp, Molecular Probes™, PS-Speck™, green http://probes.invitrogen.com/media/pis/mp07220.pdf.

2.11. Invitrogen Corp, Molecular Probes™, InSpeck Orange Intensity Calibration Kit, I7223, 0.3% intensity, http://probes.invitrogen.com/media/pis/mp07219.pdf

2.12. D. M. Haaland and R. G. Easterling, "Improved Sensitivity of Infrared Spectroscopy by the Application of Least Squares Methods," Appl. Spec. **34**, 539–548 (1980).

2.13. The signal-to-noise ratio improvements achieved through simultaneous consideration of all pixels of the image is reduced in the case where a particular component only appears in a small number of pixels, and is weak.

2.14. Invitrogen Corp, Molecular Probes™, http://probes.invitrogen.com/media/pis/mp00888.pdf?id=mp00888

2.15. J. A. Timlin, M. B. Sinclair, and D. M. Haaland, “Extending Multicolor Fluorescence Microscopy with Hyperspectral Imaging,” presented at the Pittsburgh Conference, Orlando, FL, USA, 27 Feb. – 4 Mar., 2005.

2.16. M. Ikeuchi, and S. Tabata, “Synechocystis sp PCC 6803 - a useful tool in the study of the genetics of cyanobacteria”, Photosynth. Research **70**, 73–83 (2001).

Section 3. Image Sharpening by Three Dimensional Deconvolutions

Confocal microscopes have much sharper images because most of the out of focus light from regions below and above the image plane cannot pass through the pinhole. However, as only a small fraction of the total light passes through the pinhole, the images will be very dim unless the focal plane is brightly lit, which requires the use of lasers, and is best accomplished with a scanning mirror. In this configuration, the excitation light makes a pass through the lens to illuminate a spot in the sample as described by the point spread function (PSF) of the lens. Any fluorophores within that illuminated region will emit light back through the same lens and will be detected as a spot, again described by the PSF. By passing through the lens twice, the effective PSF is the square of the lens' actual PSF, which greatly sharpens the effective PSF to give an inherently better image. Together with the use of the confocal pinhole these techniques produce excellent images.

The PSF depends critically on the light gathering capability of the lens, which is characterized by the numerical aperture (NA), and the index of refraction between the sample and the lens, where air, water, and oil can be used. Oil immersion lenses capture the more light than water, which captures more than air. High magnification, high NA, oil immersion lenses produce the narrowest PSFs, which when squared are even sharper. Even so, can the deconvolution approaches used with other microscopes improve confocal images, as well?

Castleman [3.1] says that "a confocal microscope does not require deconvolution, because it images only the structures lying within, or quite near, the focal plane." That is to say, because the effective PSF is so sharp, and the pinhole is so effective, blurring is not an issue. It is certainly true when using high magnifications, oil immersions and high numerical aperture lenses. However, when using lower magnifications the resulting PSFs are not so sharp, and image deblurring by deconvolution may be beneficial as depicted in Figure 3.1.

Images can be sharpened if the PSF is known, or can be measured, by iteratively determining a model for the light sources' locations and intensities. At each step in the process, the current light model is computationally viewed through an appropriate model lens by convolving it with the PSF to estimate what the current light distribution would look like if actually imaged. That computed image can be compared to an actual, measured image, and the differences can be used to iteratively update the light source model until the two are in agreement. There are two problems that complicate the computations and prevent the use of a direct matrix inversion to find the light. First, noise in the measurements contributes to make the matrices ill conditioned, and inversion of these matrices disproportionately amplifies the noise. Second, such inversions can result in

physically impossible light models, for instance, negative light emissions. Imposing the constraint that light sources must have nonnegative values requires different algorithms, but can easily be combined with the iterative approach [3.2].

We have implemented Agard's method, which is quite computationally intense for the size of images we collect, and further scales up by the number of frequencies used. As a result, a parallel computer code was developed. By combining this code with the Dakota optimization package [3.3], blind deconvolutions (that is, those which simultaneously estimate the lens parameters as well as the light models) are possible. However, measurement noise still contributes and limits quality of result that can be obtained.

The effect of measurement noise is particularly apparent in the spectra from deconvolved images, Figure 3.2. If one considers that the whole purpose of deconvolution is to increase the image variance (that is to sharpen the features) then it is not surprising that, in the presence of measurement noise, the deconvolved images will also have amplified effects from the noise. Also, making the original image involves a kind of averaging of point light sources over the region specified by the PSF (consider that the image is the convolution of the PSF and the light model). As a result of this averaging the original images will have smaller variances than the deconvolved light models. The spatial sharpening comes at the cost of noisier estimates of the spectral intensities. Hence, deconvolution should be used when spatial resolution in more critical than the identification of the various components in the sample's spectrum.

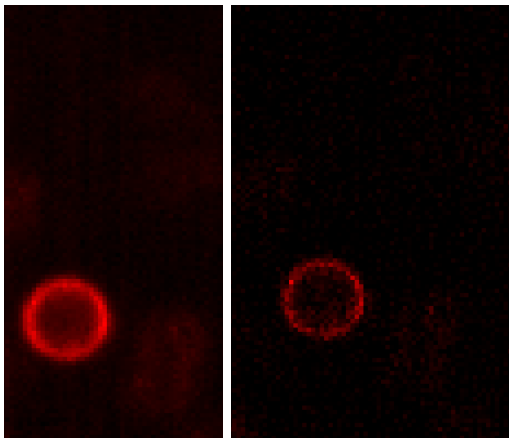

Figure 3.1. A region of interest taken from the raw image (left) and the estimated light model (right).

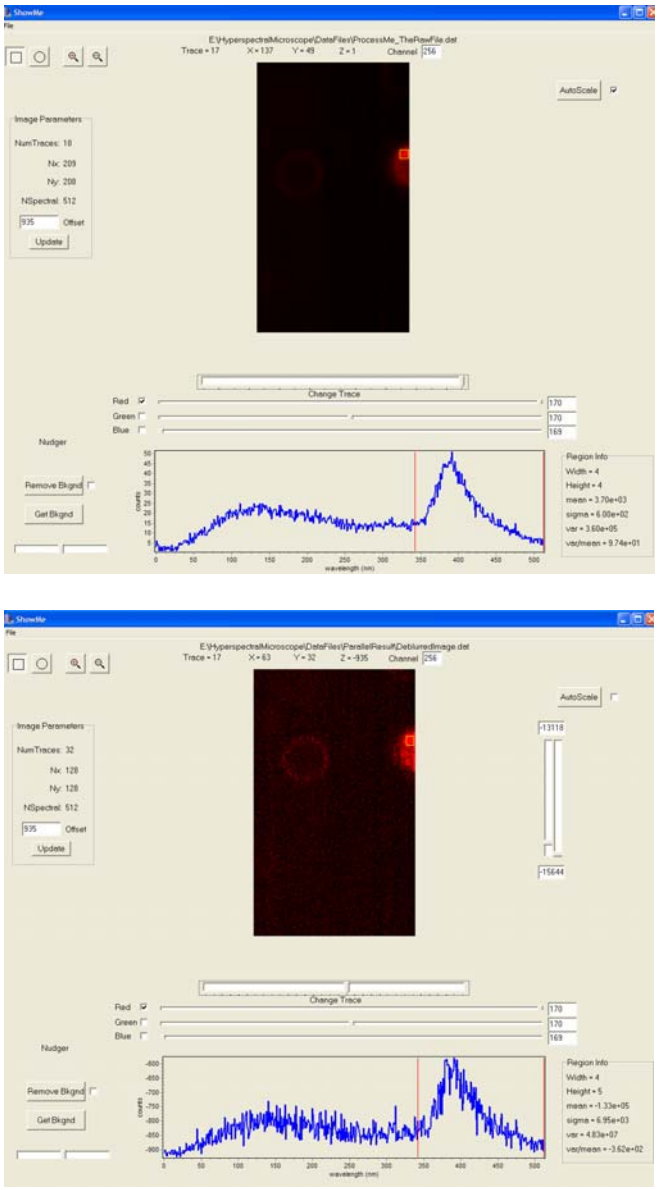

Figure 3.2. A typical spectrum from the raw image (top) and from the sharpened image (bottom).

Section 3 References

3.1 Castelman K. R., in *Confocal and Two-Photon Microscopy, Foundations, Applications, and Advances*, Alberto Diaspro, Editor, Wiley-Liss, Inc., New York, 2002, p. 248.

3.2 Agard D. A., *Optical Sectioning Microscopy: Cellular Architecture in Three Dimensions*, in *Ann. Rev. Biophys. Bioeng.* 1984, (13) pages 191-219.

3.3 Eldred, M. *et al.*, *DAKOTA, A Multilevel Parallel Object-Oriented Framework for Design Optimization, Parameter Estimation, Uncertainty Quantification, and Sensitivity Analysis Version 3.1 Users Manual*, in *SAND2001-3796*, April 2003, Sandia National Laboratories, Albuquerque, New Mexico.

Section 4. Hyperspectral Imaging Applications

Preparation and Application of Fluorescent 'Bio-beads'

In order to evaluate the spatial and spectral resolution of the 3D hyperspectral microscope for biological applications, we designed and prepared fluorescent "bio-beads". The bio-beads are micron size glass beads derivatized only on the surface to selectively bind fluorescently labeled proteins. These beads provide a well-defined biomimetic structure with similar spatial characteristics of ligand bound proteins on a cell or biological vesicle. In this model system, fluorophores are bound at well-defined and distinct locations on the surface of the microsphere, similar to that of ligands bound to an exposed receptor on the cell membrane surface. Because the fluorophores are confined to a specific location (i.e., the bead's surface) in a film of nanometer thickness (monolayer of protein), the bead is a stringent test for the spectral imager's resolution capability. Additionally, the bio-bead allows the fluorophores to maintain their environmental responsiveness and thus may be used in sensing schemes. With fluorescent beads of multiple colors embedded in a transparent medium, a simple structure can be prepared that provides an ideal test bed for the 3D hyperspectral imaging system.

Bio-beads were prepared by coupling fluorescently-labeled streptavidin protein with functionalized silica microspheres. To prepare the functionalized silica microspheres, the microspheres were first cleaned with H_2O_2/NH_4OH and then coated with an amine terminated self-assembled monolayer (SAM). The monolayer was then reacted with biotin nitrophenyl ester to generate biotin-surface-functionalized beads and fluorescent-labeled streptavidin (Molecular Probes, Inc.) was equilibrated with the functionalized beads for a few minutes to produce the completed protein-bead structure. High affinity of the streptavidin-biotin complex provides strong coupling of the protein to the bead. A series of labeled streptavidin with fluorophores having a single excitation wavelength of 496 nm but with emissions ranging from 518 – 702 nm, shown in Table 4.1, were obtained for hyperspectral imaging.

Table 4.1. Fluorescent conjugates on streptavidin

Fluorescent dye	Excitation wavelength	Emission max
Fluorescein	494	518
Oregon Green	496	524
R-Phycoerythrin	496	578
Alexa Fluor 610-R-PE	496	630
Alexa Fluor 647-R-PE	496	668
Alexa Fluor 680-R-PE	496	702

Functionalization of the Surface of Silica Microspheres:

Silica microspheres of various sizes (ranging from 160 nm to 200 μm in diameter) were purchased from Bangs Laboratories, Inc. (Fishers, IN). The microspheres were washed in a heated solution of H_2O_2/NH_4OH, rinsed in methanol, and air-dried. An amine terminated self-assembled monolayer (SAM) was then formed on the surface of the microspheres by treatment with a 10 mM chloroform solution of (3-aminopropyl) triethoxysilane (APTES). The functionalized microspheres were then exposed to a 10 mM tetrahydrofuran (THF) solution of biotin nitrophenyl ester and incubated in a warm water bath to facilitate binding of the biotin molecules to the exposed amine groups of the SAM. Finally, the beads were rinsed in fresh THF to remove any unbound biotin.

Fluorescent Labeling of the Microspheres:

Fluorescent streptavidin conjugates were purchased from Molecular Probes, Inc. (Eugene, OR). The conjugates used are as follows; Oregon Green (496 nm/524 nm), R-Phycoerythrin (496 nm/578 nm), Alexa Fluor 610-R-PE (496 nm/630 nm), Alexa Fluor 647-R-PE (496 nm/668 nm), and Alexa Fluor 680-R-PE (496 nm/702 nm).

The biotinylated microspheres were exposed to a 0.1 mg/mL phosphate buffer (PBS, pH 7) solution of streptavidin and incubated at room temperature over a 15 minute period to allow for binding of the fluorescently labeled streptavidin to the surface-immobilized biotin molecules. In order to minimize photobleaching of the fluorophores, this step as well as any subsequent handling of the resulting bio-beads was carried out in the dark. The bio-beads were then washed with fresh PBS buffer to remove any unbound streptavidin and stored in the dark at 4°C in PBS buffer until further use.

Immobilization of the Bio-beads in a Polymer Film:

In order to fix the bio-beads in three-dimensional space for imaging evaluation, the labeled beads are immobilized in a polymer matrix. Polydimethylsiloxane (PDMS) was chosen as the polymer matrix for its excellent optical transparency, compatibility with biomaterials, and a polymerization process that does not interfere with the binding of the protein and the fluorescence properties of the fluorophore conjugate. Silica microspheres coated with the labeled streptavidin were cast in a film (~200 μm thickness) of PDMS prepolymer sol. Following solidification of the PDMS and heat treatment to 60°C for a few hours, the bead's fluorescence properties were determined to have suffered no alteration in intensity or emission wavelength.

Imaging of the Bio-beads in the Polymer Film

A 2-dimensional hyperspectral confocal image of the resulting specimen is shown in Figure 4.1. This image was acquired using the 20X, NA 0.75 objective. The laser power was ~100 μW, and the exposure time was 240 μs per voxel. Interestingly, three of the labels rely on fluorescence resonance energy transfer (FRET) between closely coupled Phycoerythrin donors and Alexa acceptors. For these labels, the use of multivariate analysis also allows for separation of the residual Phycoerythrin emission from the Alexa emissions. The spectra of the beads representing the five emitting species obtained from hyperspectral image of these microspheres are also shown in Figure 4.1. The data shown in this figure provide a demonstration of the ability of hyperspectral fluorescence microscopy to image and resolve multiple labels. In this case, *five different fluorescent tags were successfully imaged in a single scan*.

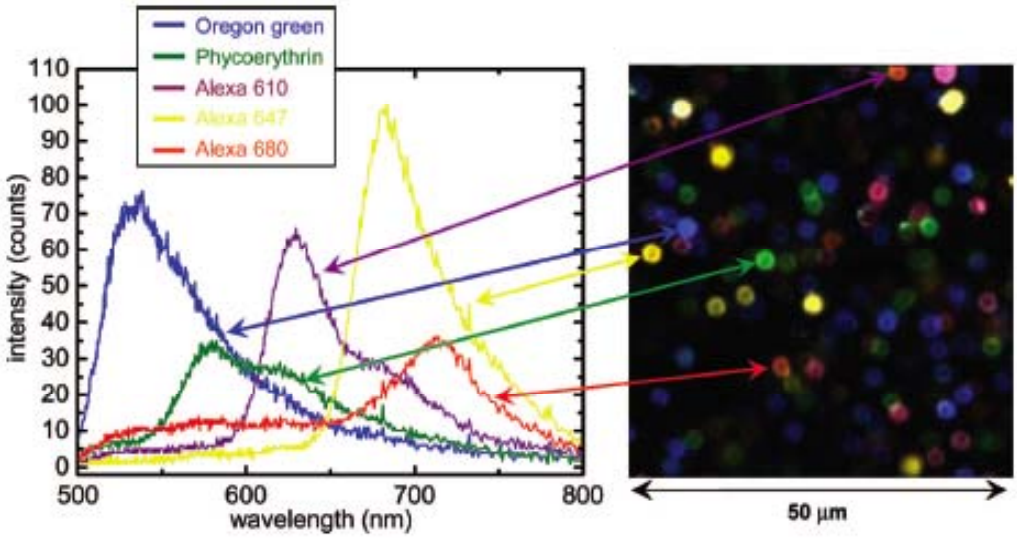

Figure 4.1. Hyperspectral image of bio beads (2.3 µm diameter) with five different streptavidin fluorescent tags. The raw emission spectra of the five compounds are shown on the left with arrows to the corresponding beads from which each spectrum was obtained. [4.1]

Supported Lipid Bilayers on Glass Microbeads

Composite architectures presenting stabilized lipid bilayers in 3-dimensional architectures are of intense current interest as platforms for biosensing, protein separations, and modeling of cellular membrane function. [4.2] A simple and viable version of this architecture is a lipid bilayer supported on a glass bead. The bilayer-coated bead approach allows us to assemble bead lattices that afford large pore volumes and high surface area for protein detection. A problem with supported lipid bilayers (SLBs), however, is the instability of the membrane under flow conditions and the strong interaction of the bilayer with the glass substrate, which inhibits membrane dynamics and alters protein function.[4.3, 4.4] Supported lipid bilayers are known to be coupled against the glass surface through weak electrostatic forces cushioned upon a 5 – 20 Å layer of water.[4.5, 4.6] The water cushion is not thick enough nor stable enough to keep membrane proteins from interacting with the glass substrate.

An approach to stabilize the SLB as well as increase the spacing between the substrate and the bilayer is through the use of lipid tethers. Previous research in this area has focused on thiol-gold tethered systems, which rely on surfaces being gold-coated.[4.7, 4.8] Development of a silane-coupled film would greatly expand the surfaces and devices upon which the tethered bilayers could be configured upon. We have recently developed a new methodology and chemistry to generate a tethered membrane architecture using mild reaction

conditions. The tether molecules are amine-terminated oligoethylene glycols that are appended to hydrophobic lipid bodies. Examples are shown in Figure 4.2. Formation of a glycidoxy monolayer film through standard silane coupling chemistry provides a surface upon which the tether molecule can then be linked to the silica surface through the reaction of the amine from the tether and the epoxide of silane film. Figure 4.3 shows the step-by-step process of forming the glycidoxy silane, followed by tether coupling and ethanol amine backfilling of unreacted epoxides, and then formation of the SLB through spontaneous vesicle fusion.

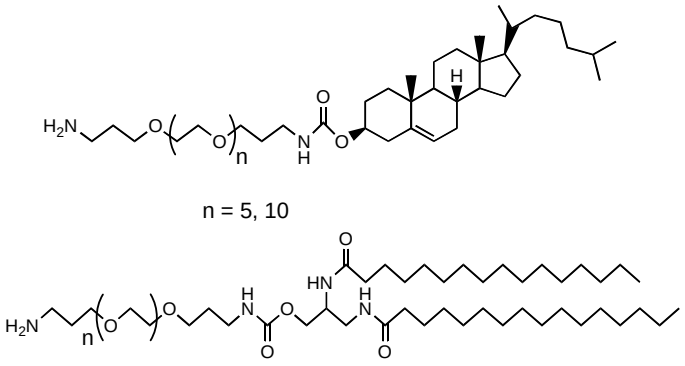

Figure 4.2. Tether molecule structures. The amine terminal group provides a reactive end to covalently couple to surface functionality, while the oligoethylene glycol unit acts a hydrophilic spacer and the lipid body serves as the lipid bilayer anchor.

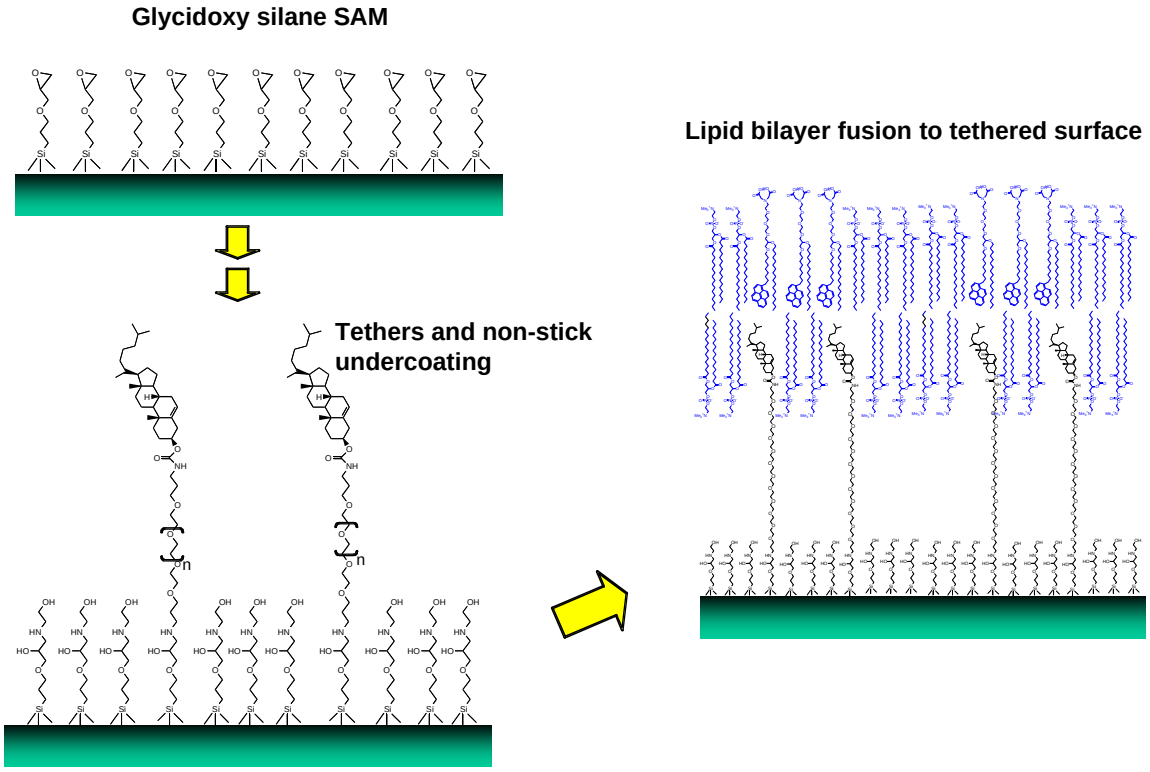

Figure 4.3. Stepwise formation of the tethered SLB. A self-assembled monolayer (SAM) of a glycidoxy silane is first formed through standard silane coupling to a glass surface. The tether molecules are then covalently attached to the surface followed by backfilling with ethanolamine. The final step couples the lipid bilayer via vesicle fusion to form the SLB.

The tether molecules are designed to 1) react with a functionalized coating through a non-polymerizing endgroup, 2) insert and anchor into the lipid bilayer through the lipid body, and 3) separate the bilayer from the substrate surface through a hydrophilic spacer unit. Siloxane endgroups on tether molecules are commercially available but have difficulty in reproducibility of generating specific tether densities due to the self-reactivity of the silane. The amine functionality does not self-react and thus can be stored for long periods of time. Additionally, it is selective in reactivity for specific functional groups allowing more flexibility in the tailoring of surfaces. The hydrophilic spacer is an oligoethylene glycol that can be extended to any desired length. This spacer will allow us to vary the surface-bilayer separation for optimal protein-membrane behavior and membrane stability. The lipid body can be one of many structures, but typical structures found in cellular membranes include phospholipids, sphingolipids, and cholesterol. Through hydrophobic and van der Waals interactions these lipid bodies on the tether molecules should spontaneously insert into the lipid membrane during the vesicle fusion process.

Our first version of the tether molecule was prepared by reacting diamino oligoethylene glycols with cholesteryl chloroformate. Cholesterol tether molecules with pentaethylene glycol (Chol-DPA200E) and decaethylene glycols (Chol-DPA400E) were prepared and isolated using a tandem separation process of a basic alumina column followed by a silica gel column to purify the free base. The colorless waxy product yielded ^{1}H NMR and Fourier transform infrared (FTIR) spectral data and elemental analysis data indicative of the proposed structure.

Preparation of the tethered coated glass beads was accomplished using standard silane coupling and surface functionalization procedures. In brief, the glass beads (30 – 50 microns) were cleaned using piranha solution (25% H_2O_2 solution/H_2SO_4), cleaned through a series of washing steps, and then placed in a solution of 3-glycidoxypropyl trimethoxysilane (20 mM) in anhydrous tetrahydrofuran (THF) for one hour at room temperature. The beads were then rinsed several times with fresh THF and immediately placed in a solution of the tether molecule (1 mM) in anhydrous THF for various time periods spanning from 10 minutes to 16 hours at room temperature to vary the density of surface bound tethers. After the beads were recovered and rinsed several times with fresh THF, they were placed in a solution of either aminoethanol or triethylene glycol to backfill the unreacted glycidoxy groups for 16 hours at room temperature. As the final step the beads were isolated and washed several times with THF, followed by methanol, then dried under vacuum at 60 °C overnight. Formation of the SLB on the tethered beads was achieved by simply flowing lipid vesicles (liposomes) over the bead surface and allowing spontaneous vesicle fusion to occur. Figure 4.4 shows a schematic of the tethered SLB glass bead.

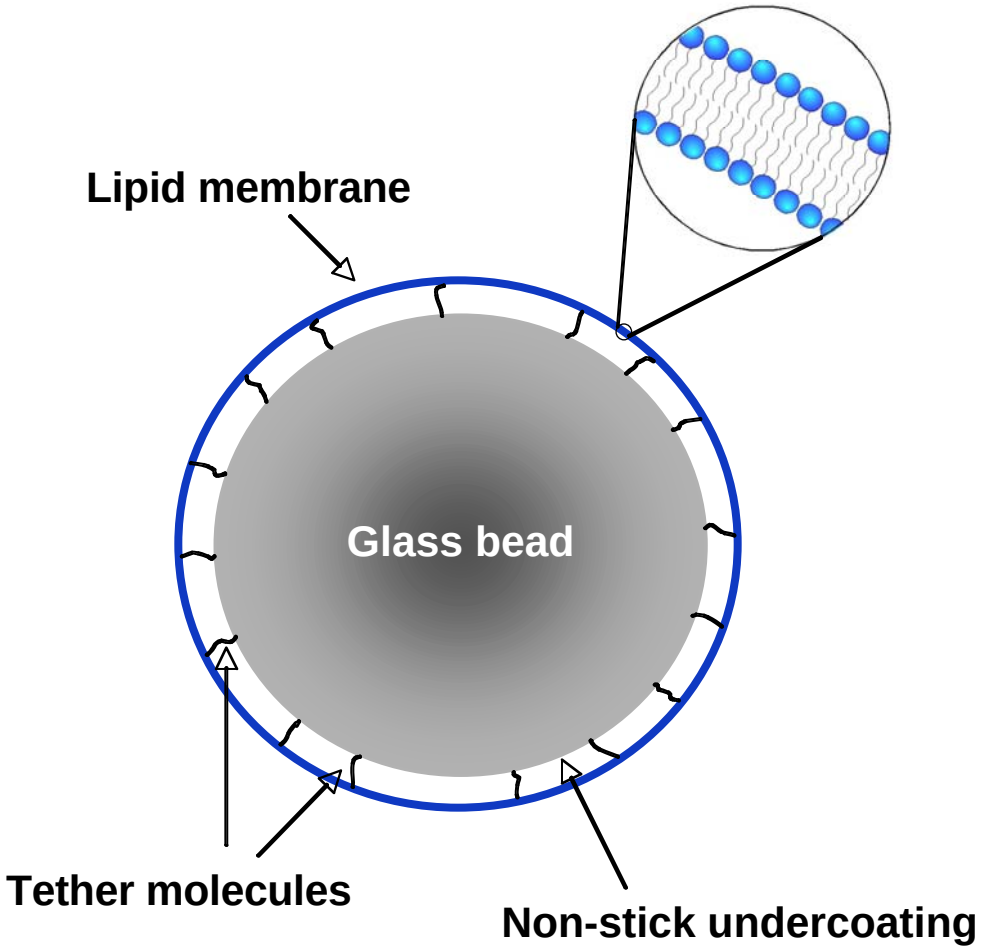

Figure 4.4. Schematic of the tethered supported lipid bilayer on a glass bead.

The first versions of the tethered beads were coupled with bilayers of 5% PSIDA/ distearylphosphatidyl choline (DSPC) doped 0.5 mole % of NBD-PE (λ_{ex} = 463 nm, λ_{em} = 536 nm). Imaging of the beads was accomplished through the mylar cover and 1 mm of buffered water in a perfusion cell using a 20X objective. Images obtained with the hyperspectral microscope revealed that the SLB formed poorly on the tethered surface with a patchy appearance (Figure 4.5, left image). By comparison, the SLB on plain glass beads was uniformly distributed over the bead surface (Figure 4.5, right image). With these structures, we attempted to produce a 3D image of a bilayer coated bead. Although the top half of the structure can be obtained with good resolution, we found that the lower half of the structure could not be resolvable due to issues of refracted and trapped light in the glass bead.

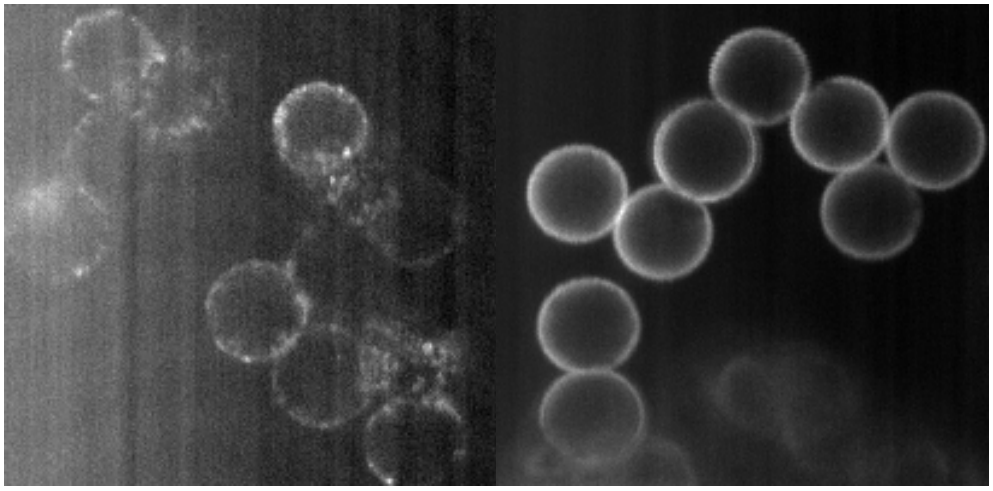

Figure 4.5. Hyperspectral 3D imaging of bilayer coated beads with (left) and without (right) a tethered surface.

The poor bilayer coating observed with the tethered bead was indicative of a problem in the coating procedure. One area of concern was the settling of the beads in the coating solutions that could lead to inhomogeneous reactivity over the bead surface. Continuous suspension of the beads during all coating steps should yield homogeneous functionalization of the surface. Such suspension of the beads was achieved by shaking the bead containing solution on a vortex shaker at low vortex speed. The silane coupling, tether attachment, and backfilling steps were all performed with the shaker. Bilayers of eggPC doped with 0.5% NBD-PE were found to couple as a uniform SLB on the tethered coated bead with no difference in homogeneity detected from the plain glass bead. A fluorescence image from the 3D hyperspectral imager of a tethered bilayer is shown in Figure 4.6. We are currently tailoring our surfaces regarding tether density and backfiller to achieve optimal membrane behavior and membrane stability on the bead surface.

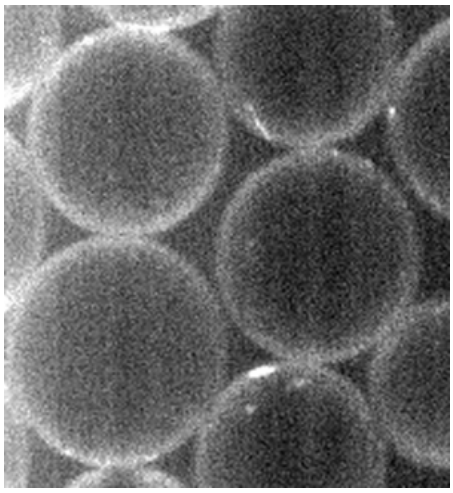

Figure 4.6. 3D hyperspectral image of tethered beads of eggPC with 0.5% NBD-PE.

Imaging of Synechocystis Cyanobacteria

To demonstrate the application of the new microscope to biological imaging, in-vivo hyperspectral images of the cyanobacteria *Synechocystis* sp. PCC 6803 [4.9] were obtained. The bright fluorescent emission exhibited by these organisms is due to a number of native photosynthetic pigments (e.g., phycobilins, chlorophyll) occurring within the ~2 μm diameter cell. These pigments are highly overlapped, both spatially and spectrally: no single voxel contains only one emitter, and no isolated emission bands occur. Hyperspectral data was acquired using the 60X, NA 1.4 objective, with an excitation power of 20 μW, and an exposure time of 240 μs. Figure 4.7 shows the ~42,000 spectra obtained from a single x-y slice of a 3-dimensional image along with a 2-dimensional grey scale integrated image of a group of *Synechocystis* cells. The ensemble of single pixel spectra was analyzed using our MCR software to determine the pure-emission spectrum of each emitting component and the relative concentrations of the emitting species for each pixel of the image. The multivariate analysis revealed that the entire hyperspectral image stack could be modeled using linear admixtures of six emitting species. The figure also shows the 6 pure emission sources in the image along with the relative concentration maps of each emitting component. The RGB image shown in Figure 4.7 was obtained by color coding and combining the concentration maps of all six emitting species. Finally, spectra and MCR fits to those spectra are also shown for three individual pixels in the image to demonstrate the quality of the fits and the heterogeneity of the component concentrations within and between Synechocystis cyanobacteria. The data shown in Figure 4.7 confirm that hyperspectral confocal microscopy is a powerful technique that can be used to simultaneously follow multiple fluorescent tags. Finally, the figure also shows a

rendered image based upon the MCR-derived concentrations and further demonstrates the heterogeneity of the cells. The results shown in the figure reveal that the maximum benefit of the hyperspectral approach is achieved through a close coupling of the hyperspectral imaging hardware and the multivariate data analysis. The spectra of the six photosynthetic pigments occurring in the *Synechocystis* cells are highly overlapped spectrally: five of the six emission peaks occur within a ~50 nm spectral range. No filter based instrument is capable of separating a group of four such closely spaced spectra utilizing a single scan. Furthermore, the emitting components are spatially overlapped within the cell: all pixels in the hyperspectral image contain the contribution from multiple emitters. The MCR algorithms are capable of separating such spatially and spectrally overlapping components, provided that the spectra are not identical for any pair of emitting species and that pixel-to-pixel variations in relative contributions of the emitting species occur somewhere within the image.

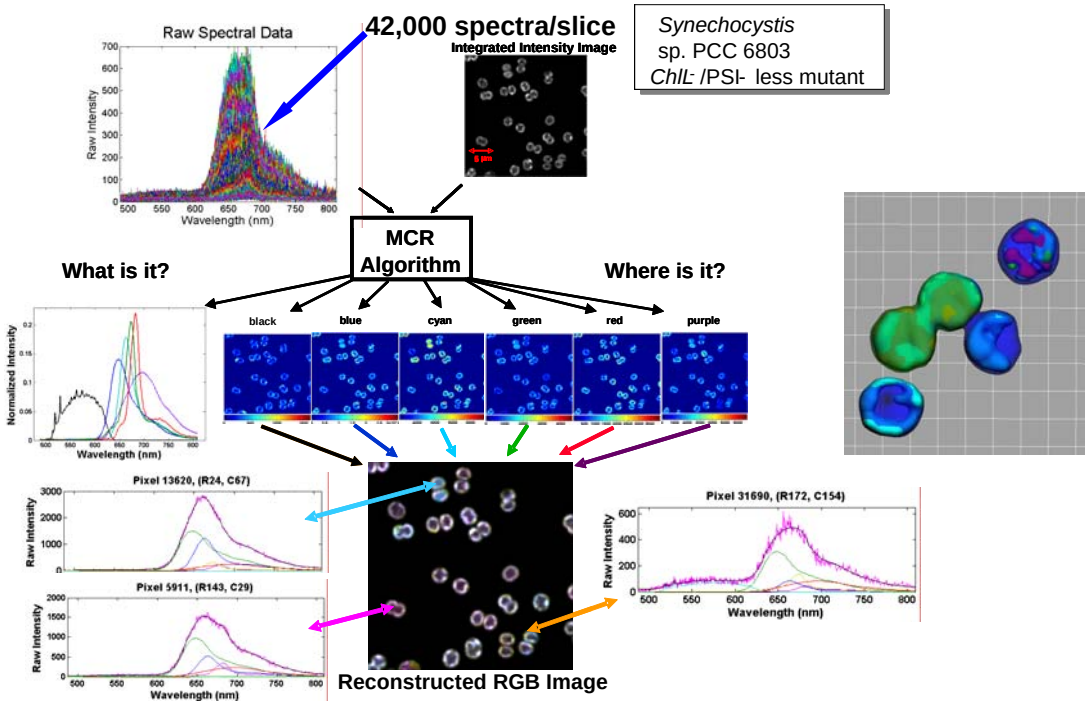

Figure 4.7. Series of spectra from a 2D image plane of mutant *Synechocystis* bacteria demonstrating the pure emission spectra and the concentration maps derived from the application of the MCR algorithm to the spectral data. The composite RGB image is presented along with the spectra and fitted data from three individual pixels demonstrating quite different relative concentrations of the pigments in each pixel and cell. The inset image is a rendered 3D image of a few cells demonstrating the high heterogeneity of the pigments both within and between the cells. The background grid spacing of the inset represents 1 µm increments.

Microtubules and Motor Proteins

This year's goal was to develop and image three-dimensional assemblies of microtubules and fluorescently tagged kinesin motor proteins. In FY05, we demonstrate the ability to artificially assemble 3D microtubule networks organized on an "artificial centrosome." Attachment and movement of tagged kinesin, however, proved to be problematic. Thus, in FY06 we pursued a different tract: harnessing the intact microtubule networks from living cells.

The cytoskeletal networks were extracted from two model cell lines, rat neuronal cells (B35) and human liver cells (HeLa). Cells were grown to 80 – 100% confluency on glass coverslips in 6-well plates. Coverslips were removed from the plates, washed once with 1x PBS (phosphate buffered saline). The coverslips were then incubated with extraction buffer (BRB80 + 4mM EGTA + 0.5% TX-100 + ATP [1mM-100mM]) for 30 sec, and fixed with cold methanol (-20˚C) for 3 min. The fixed microtubule networks were then stained using a fluorescent antibody. Briefly, the coverslips were rehydrated with 1x TBS (Tris buffered saline) + 0.1% Triton X-100, and then incubated with a 1:100 dilution of mouse anti-$\alpha\beta$ tubulin antibody in 1x TBS + 0.1% Triton X-100 + 2% BSA for 2 hours in the dark at 25°C. Coverslips were washed three times with TBS, and incubated with a 1:100 dilution of an anti-mouse, Alexa Fluor 488 for 1 hour in the dark at 25°C. The coverslips were then washed three times with TBS, and mounted on glass slides using Cytoseal. Images were acquired with an Olympus IX-71 inverted microscope and Hamamtsu Ocra ER CCD camera.

The functionality of the microtubule networks were evaluated using kinesin-based bead assays. In these experiments, the microtubule networks were stained using a fluorescently tagged derivative of taxol, a small organic molecule that binds and stabilizes microtubules. Kinesin-coated microspheres (500 nm and 200 nm) and semiconductor quantum dots were incubated in BRB80 + 1 mM ATP + 0.5 mg/mL casein at 4°C for 10 min. Microspheres were then incubated in a solution of *Drosophila* kinesin motor proteins for 15 min at 4°C. Kinesin-coated beads were then introduced into flow cells containing the fixed microtubule networks.

Results:

Intact microtubule networks were successful prepared from both the HeLa and B35 cells. An example of the HeLa cell network, stained with the Alexa Fluor 488 conjugate, is shown in Figure 4.8A. Fluorescence microscopy demonstrated the removal of the cell membrane, as well as intracellular organelles and actin cytoskeleton, while maintaining the intact microtubule network. This methodology enables the synthesis of 3D microtubule networks for nanotechnological applications. A key advantage to this method over those previous developed in FY05 is the ability to synthesize highly dense and interconnected microtubule networks.

Implementation of these microtubule networks in bead-based, kinesin motility assays was problematic. Attachment of kinesin-coated fluorescent microspheres and quantum dots was observed (Figure 4.8B), but movement was not demonstrated. Potential factors limiting transport include the presence of microtubule-associated proteins such as Tau, and excess crosslinking of tubulin molecules, which inhibits kinesin movement along the microtubules. In addition, background fluorescence from unattached kinesin-coated quantum dots (and microspheres) hindered observation.

(A) **(B)**

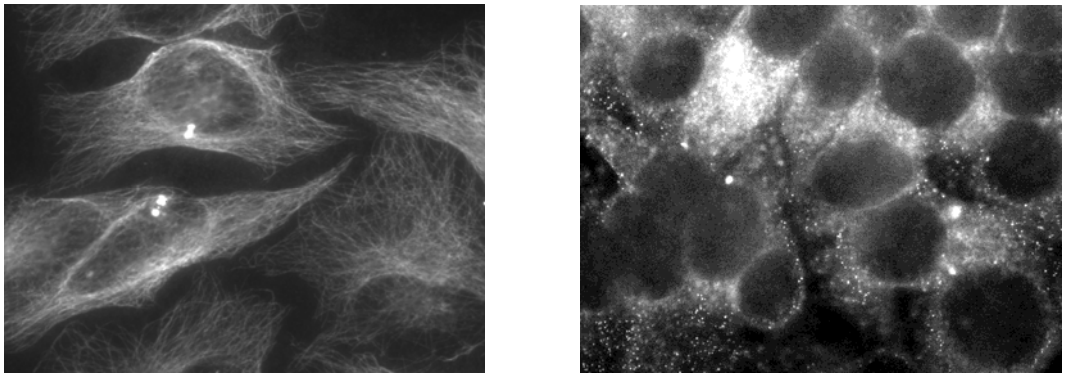

Figure 4.8: (A) Fixed microtubule networks extracted from human liver (HeLa) cells and stained with a Alexa Fluor 488 conjugated antibody. (B) Microtubule networks from HeLa cells with kinesin-coated quantum dots attached.

Section 4 References

4.1 Sinclair, M. B., D. M. Haaland, J. A. Timlin, and H. D. T. Jones *Appl. Optics* **45**(24):6283 – 6291 (2006).

4.2 E. Sackmann, E. *Science* **271**, 43 (1996).

4.3 McConnell, H. M., T. H. Watts, R. M. Weis, A. A. Brian, *Biochim. Biophys. Acta* **864**, 95 (1986).

4.4 Salafsky, J., J. T. Groves, S. G. Boxer, *Biochemistry* **35**, 14773 (1996).

4.5 Koenig, B. W., S. Krueger, W. J. Orts, C. F. Majkrzak, N. F. Berk, J. V. Silverton, K. Gawrisch, *Langmuir* **12**, 1343 (1996).

4.6 Bayerl, T. M., M. Bloom, *Biophys*. *J*. **58**, 357 (1990).

4.7 Cheng, Y., N. Boden, R. J. Bushby, S. Clarkson, S. D. Evans, P. F. Knowles, A. Marsh, R. E. Miles, *Langmuir* **14**, 839 (1998).

4.8 Williams, L. M., S. D. Evans, T. M. Flynn, A. Marsh, P. F. Knowles, R. J. Bushby, N. Boden, *Langmuir* **13**, 751 (1997).

4.9 Ikeuchi, M., S. Tabata, *Photosynth. Research* **70**, 73 (2001).

Section 5. Trilinear Modeling of Time-resolved Hyperspectral Images

Time-resolved hyperspectral images yield an opportunity to analyze the images in a manner that reduces rotational ambiguity in the data. If the data set is trilinear (i.e., it can be factored into the product of three matrices) then new opportunities exist for analysis of the hyperspectral images. This section describes these new analysis approaches for trilinear data.

In its native data acquisition mode, the 3D hyperspectral microscope [5.1] collects notional bilinear data. That is, for an *r*-component chemical system, the data follow the model

$$f_{ij} = \sum_{p=1}^{R} c_{pi} s_{pj} \tag{1}$$

where f_{ij} is the fluorescence intensity at pixel *i* and wavelength *j*, c_{pi} is the concentration, or relative amount of the p^{th} fluorophore at pixel *i*, and s_{pj} is the unit-concentration fluorescence response for the p^{th} fluorophore at wavelength *j*. Rewriting this relationship in matrix terms yields

$$\mathbf{F} = \mathbf{C}\mathbf{S}^{T}, \tag{2}$$

where **F** is the $i \times j$ matrix of fluorescence intensities, **C** is the $i \times r$ matrix of concentrations, and **S** is the $j \times r$ matrix of fluorescence responses. In this research, we analyze the data in **F** using MCR. Briefly, the matrices **C** and **S** are alternately estimated using multivariate least squares while employing constraints. Tucker [5.2] employed a notation that utilized pre-subscripts and post-subscripts of a matrix to designate the modes of its row and column information. Thus the matrix equation (2) can be written as,

$${}_{i}\mathbf{F}_{j} = {}_{i}\mathbf{C}_{r}\left({}_{j}\mathbf{S}_{r}\right)^{T} = {}_{i}\mathbf{C}_{r}\mathbf{S}_{j}. \tag{3}$$

Clearly, the transpose operator can now be represented as a change in subscripts. Now, when we add an additional acquisition mode, temporal photodegradation, that varies linearly as do the concentration and wavelength modes, the 3D hyperspectral microscope can collect notional trilinear data.

Trilinear data follow the model,[3-8]

$$f_{ijk} = \sum_{p=1}^{R} c_{pi} s_{pj} t_{pk}, \tag{4}$$

where f_{ijk} is the f_{ij} measured at the k^{th} time interval and t_{pk} is the concentration-independent photodecomposition rate for fluorophore *p* evaluated at time interval *k*. In order to facilitate understanding we utilize the *vec* operator[9]. The *vec* operator transforms an $i \times j$ matrix into an $ij \times 1$ vector such that each column, *j*, is appended to the last element of the preceding column. For our matrix ${}_{i}\mathbf{F}_{j}$ whose columns are the length *i* vectors ${}_{i}\mathbf{f}(1)$, ${}_{i}\mathbf{f}(2)$, through ${}_{i}\mathbf{f}(j)$, we have

$${}_{i}\mathbf{F}_{j} = \left[{}_{i}\mathbf{f}(1) \quad {}_{i}\mathbf{f}(2) \quad \cdots \quad {}_{i}\mathbf{f}(j)\right],$$

and

$$vec({}_i\mathbf{F}_j) = \begin{bmatrix} {}_i\mathbf{f}(1) \\ {}_i\mathbf{f}(2) \\ \vdots \\ {}_i\mathbf{f}(j) \end{bmatrix} = {}_{ij}\mathbf{F}_1 = {}_{ij}\mathbf{f} \ .$$

To avoid confusion with dimensionality, we denote indexing of vectors and matrices parenthetically. Collecting our trilinear data as a set of matrices, ${}_i\mathbf{F}_j(1)$ through ${}_i\mathbf{F}_j(k)$, conceptually, they would be organized as a deck of cards,

$$\mathbb{F} = \left[{}_i\mathbf{F}_j(1) \middle| {}_i\mathbf{F}_j(2) \middle| \cdots \middle| {}_i\mathbf{F}_j(k) \right], \tag{5}$$

where the fancy F is now a three-way array. It is fairly straightforward to convert F into a matrix, which we can employ in a least squares way. We perform this transformation using the *vec* operator on each matrix in the array, *viz*,

$$\mathbb{F} \Rightarrow {}_{ij}\mathbf{F}_k = \left[vec\left({}_i\mathbf{F}_j(1)\right) \quad vec\left({}_i\mathbf{F}_j(2)\right) \quad \cdots \quad vec\left({}_i\mathbf{F}_j(k)\right) \right] \tag{6}$$

We will utilize the matrix ${}_{ij}\mathbf{F}_k$ to solve for the temporal data in ${}_k\mathbf{T}_R$. But first, we want to form the two other matrix arrangements of F. These are easily generated using a cyclic permutation of ${}_{ij}\mathbf{F}_k$, involving only a transpose operation and index reassignment. Specifically, they are

$${}_{ki}\mathbf{F}_j = {}_{ki}\left({}_k\mathbf{F}_{ij}\right)_j \ , \tag{7}$$

$${}_{jk}\mathbf{F}_i = {}_{jk}\left({}_j\mathbf{F}_{ki}\right)_i \ , \text{ and} \tag{8}$$

$${}_{ij}\mathbf{F}_k = {}_{ij}\left({}_i\mathbf{F}_{jk}\right)_k \ . \tag{9}$$

Equations (7) and (8) give the matrices employable for the solution of ${}_j\mathbf{S}_r$ and ${}_i\mathbf{C}_r$, respectively. Note that the indices rotate across the parentheses from the left and move from the right hand side to the far left position. Equation (9) regenerates the matrix in Eq. (6) and is included to show the completion of the cycle. In terms of computational demand, the most costly part of the permutations above is the transpositions. Those familiar with Matlab may recognize the index reassignment as a *reshape* operation. Having constructed the matrices in Eq. (6), (7) and (8), we will now construct the conformable matrices needed to make the least squares estimates of **C**, **S** and **T**.

Although some authors use core matrices and tensor notation [5.10,5.11, we prefer to keep the ideas on the level of matrices since it is more compatible with the computational procedures and algorithms used in least squares. With this in mind, we use the Khatri-Rao operator[5.12], designated $\bullet$. The Khatri-Rao operator performs the *vec* operation [5.12] on the outer product (i.e., $\mathbf{cs}^T$) of *each* column of the pair of matrices on which it operates. The following equation provides an example.

$${}_i\mathbf{C}_r \bullet {}_j\mathbf{S}_r = \left[vec\left({}_i\mathbf{c}(1)\mathbf{s}_j(1)\right) \quad vec\left({}_i\mathbf{c}(2)\mathbf{s}_j(2)\right) \quad \cdots \quad vec\left({}_i\mathbf{c}(r)\mathbf{s}_j(r)\right) \right]$$

Now we can generate the conformable matrices to apply to the models:

$$ {}_{ij}\mathbf{F}_k = {}_{ij}\mathbf{X}_r \mathbf{T}_k , \tag{10} $$

$$ {}_{ki}\mathbf{F}_j = {}_{ki}\mathbf{Y}_r \mathbf{S}_j , \tag{11} $$

$$ {}_{jk}\mathbf{F}_i = {}_{jk}\mathbf{Z}_r \mathbf{C}_i ; \tag{12} $$

with

$$ {}_{ij}\mathbf{X}_r = {}_i\mathbf{C}_r \bullet {}_j\mathbf{S}_r , \tag{13} $$

$$ {}_{ki}\mathbf{Y}_r = {}_k\mathbf{T}_r \bullet {}_i\mathbf{C}_r , \tag{14} $$

$$ {}_{jk}\mathbf{Z}_r = {}_j\mathbf{S}_r \bullet {}_k\mathbf{T}_r . \tag{15} $$

Note the cyclic nature of right hand side matrices in Eq. (13), (14) and (15). Finally, we are ready to estimate **C**, **S** and **T** from Eq. (10), (11) and (12). Using multivariate least squares, the estimates are

$$ {}_r\hat{\mathbf{T}}_k = \left({}_r\mathbf{X}_{ij}\mathbf{X}_r \right)^{-1} {}_r\mathbf{X}_{ij}\mathbf{F}_k , \tag{16} $$

$$ {}_r\hat{\mathbf{S}}_j = \left({}_r\mathbf{Y}_{ki}\mathbf{Y}_r \right)^{-1} {}_r\mathbf{Y}_{ki}\mathbf{F}_j , \tag{17} $$

$$ {}_r\hat{\mathbf{C}}_i = \left({}_r\mathbf{Z}_{jk}\mathbf{Z}_r \right)^{-1} {}_r\mathbf{Z}_{jk}\mathbf{F}_i . \tag{18} $$

Of course, as in MCR, the estimates from the previous iteration are returned for use in the present iteration. While there seems to be much matrix manipulation, trilinear decomposition (TLD) is only modestly more complicated than MCR.

All of our computations were performed on a Pentium 4, 3.20 GHz-based PC with 1 gigabyte of RAM. Our algorithms and programs were written at Sandia National Laboratories and run in Matlab®.[5.13] We applied TLD to a 3D hyperspectral microscope image array. The array imaged a plate containing a group of cells, one modified with yellow fluorescent protein (YFP). The cells were subject to photodegradation by repeated imaging for 18 iterations. The final image size was 209 × 208 pixels × 512 wavelength elements × 18 temporal elements. The image array was stored as a matrix oriented as pixel-pixel-temporal × wavelength (782496 × 512 elements).

After acquisition, we performed a 64-factor, principal component analysis (PCA) on the digital image in order to reduce it to a more manageable size. Following PCA we trimmed noisy edge pixels, reducing the image to 200 × 200 pixels. Prior to TLD, we binned the data (Haar-Walsh wavelet compression [5.14]) in the image plane, further reducing the image to 25 × 25 pixels, for a total of 625 pixels. So, now our trilinear data is dimensioned 625 × 512 × 18, as $i \times j \times k$.

Our first data analytical task was to estimate the rank of the data. This is a challenging undertaking with bilinear data, and not well understood with trilinear data. There are several published suggestions for rank estimation; however, we chose to use an extension of one of the bilinear methods. With bilinear data one can estimate rank by performing PCA on the data and examining the magnitude

of the eigenvalues. We sort the eigenvalues from largest to smallest and plot them sequentially on a semi-log scale. The index at which the eigenvalues flatten out, we identify as the first noise component and all previous eigenvalues are signals. To obtain eigenvalues for our trilinear data, we performed PCA on each of the three matrices in Eq. (10), (11) and (12), *i.e.*,

$$ {}_k\mathbf{F}_{ij}\mathbf{F}_k = {}_k\mathbf{P}_R\boldsymbol{\Sigma}_R\mathbf{P}_k \,, \tag{19} $$

$$ {}_j\mathbf{F}_{ki}\mathbf{F}_j = {}_j\mathbf{Q}_R\boldsymbol{\Lambda}_R\mathbf{Q}_j \,, \tag{20} $$

$$ {}_i\mathbf{F}_{jk}\mathbf{F}_i = {}_i\mathbf{R}_R\boldsymbol{\Pi}_R\mathbf{R}_i \,. \tag{21} $$

$\boldsymbol{\Sigma}_R$, $\boldsymbol{\Lambda}_R$, and $\boldsymbol{\Pi}_R$, are diagonal matrices containing the eigenvalues of their respective cross-product matrices and R represents the mathematical rank of each of the cross-products. We expect that for real data, R would equal i, j, or k, for the respective cross-products. Figure 5.1 presents the eigenvalues of the three modes of our 3D hyperspectral microscope image data. Inspection of the plots indicates that the rank of the data is three for each of the three modes.

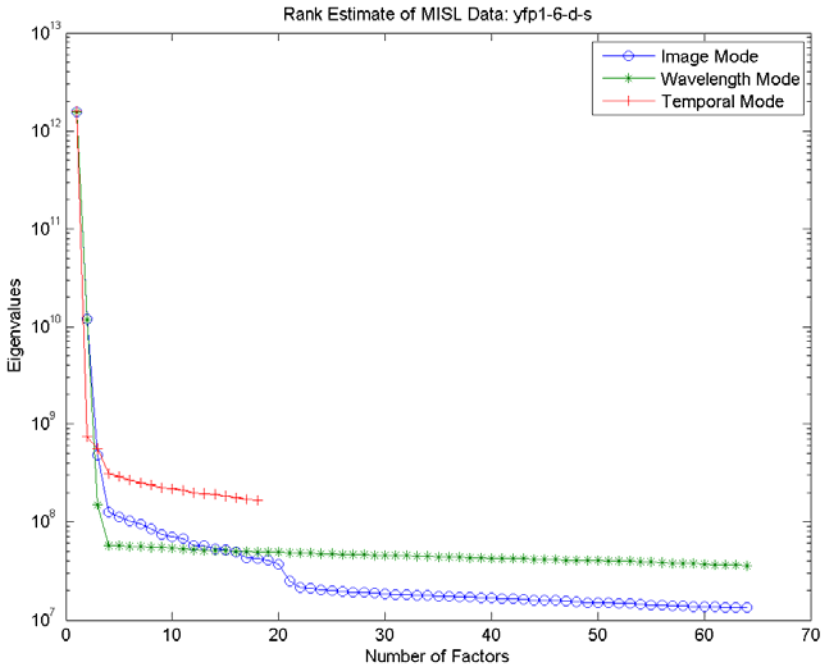

Figure 5.1. Eigenvalues of 3D hyperspectral microscope image array. Blue, green, and red are the image, wavelength and temporal modes, respectively. From each of the modes, we infer a rank-three array.

Using the rank-three estimate, we conducted our TLD of the data. Our analysis involved an alternating least squares scheme as explained in Eqs. (16), (17), and (18), in that order. Initial estimates for the elements of matrices ${}_i\mathbf{C}_3$ and ${}_j\mathbf{S}_3$ were random values selected from a uniform, positive distribution. Termination criteria was based on the route-mean square error between the data and the estimate, determined as

$$RMSE = \left(\left\| {}_{ij}\mathbf{F}_k - {}_{ij}\mathbf{X}_r \mathbf{T}_k \right\|_F^2 \right)^{1/2}. \quad (22)$$

The algorithm terminated when two successive values of the RMSE differ by less than machine precision times 10^5.

We employed a rigorous least squares nonnegativity constraint [5.15] to the first 200 iterations of the TLD to preclude two-factor degeneracy. Figure 5.2 contains the rank three resolution of the TLD. Component 2 in the wavelength mode shows the typical broad, featureless autofluorescence (AF) spectrum centered near 560 nm. There also appears to be a redundant, but slightly shifted, YFP peak at around 530 nm in components 1 and 3. This was a somewhat surprising and disappointing result. Our expectation for these data, based on our knowledge of the sample and previous analyses from this system, was three distinct components: the YFP, the AF and an essentially flat dark-current offset. Higher ranked decompositions produced similar results with multiple redundant factors. We then inspected the residuals from the TLD model.

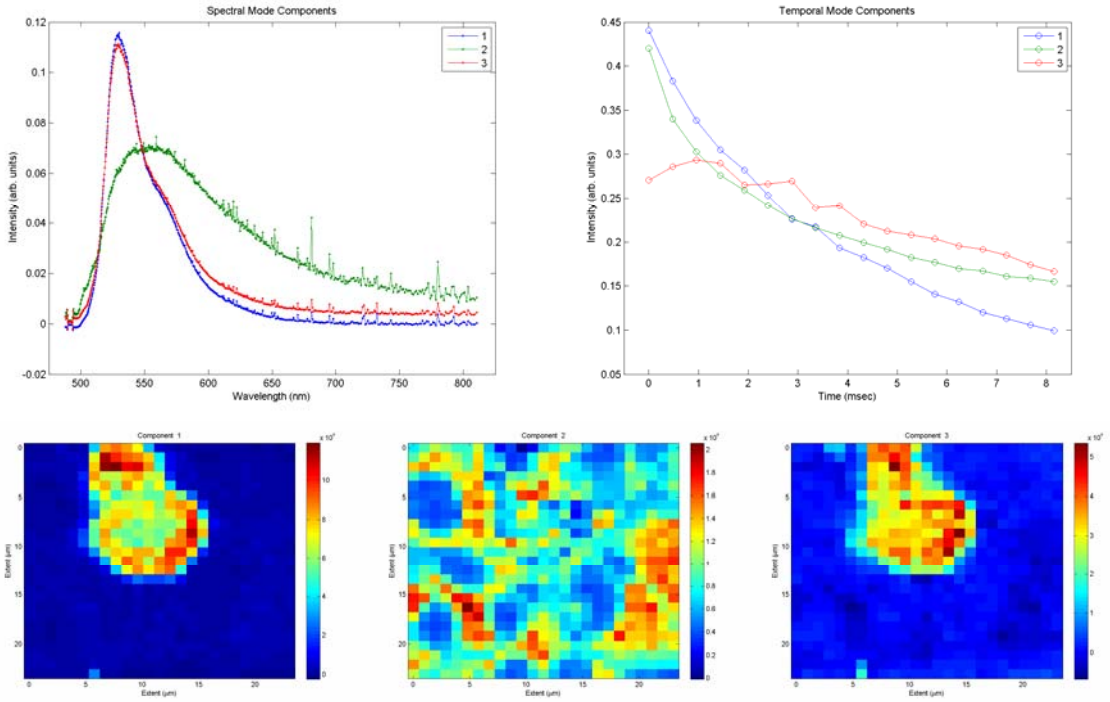

Figure 5.2. Compressed, 3D hyperspectral microscope data using three component model TLD. Top L-R: Three component model spectral profiles and temporal profiles. Bottom L-R: Image mode for each of the three components.

The rank three TLD model left highly structured residuals in the wavelength mode with peaks similar to YFP. PCA of the residuals showed structure in the wavelength mode of the first three residual components. The temporal and image modes also produced highly structured and distinguishable residuals. We interpreted this as either the inadequacy of the trilinear model or that the noise structure of the data precluded a sufficient fit to the data. Previous analyses of

comparable data indicated a Poisson or multiplicative noise structure. In light of this, it was appropriate to scale the data prior to analysis to account for noise.

In two-way analyses, noise scaling for Poisson distributed noise can be approximated using the mean of each mode.[5.16] For example, we can compute the mean of the row space of the bilinear data, **F**, as

$$ {}_{i}\mathbf{\Phi}_{i} = \frac{1}{j} diag\left({}_{i}\mathbf{F}_{j}\mathbf{1} \right), $$

where $\mathbf{\Phi}$ is a diagonal matrix with the mean of each row as its diagonal elements and **1** is a column vector of ones. Likewise, the column space means are contained in $\mathbf{\Psi}$ using

$$ {}_{j}\mathbf{\Psi}_{j} = \frac{1}{i} diag\left(\mathbf{1}_{i}\mathbf{F}_{j} \right), $$

We can incorporate $\mathbf{\Phi}$ and $\mathbf{\Psi}$ into the scaling method using the inverse of their square roots,

$$ {}_{i}\tilde{\tilde{\mathbf{F}}}_{j} = {}_{i}\mathbf{\Phi}^{-1/2}\,{}_{i}\mathbf{F}_{j}\,\mathbf{\Psi}_{j}^{-1/2}. $$

If we merely extend this strategy into the third mode and define $\mathbf{\Phi}$, $\mathbf{\Psi}$, and $\mathbf{\Omega}$ as

$$ {}_{i}\mathbf{\Phi}_{i} = \frac{1}{jk} diag\left(\mathbf{1}_{jk}\mathbf{F}_{i} \right), \tag{23} $$

$$ {}_{j}\mathbf{\Psi}_{j} = \frac{1}{ki} diag\left(\mathbf{1}_{ki}\mathbf{F}_{j} \right), \text{ and} \tag{24} $$

$$ {}_{k}\mathbf{\Omega}_{k} = \frac{1}{ij} diag\left(\mathbf{1}_{ij}\mathbf{F}_{k} \right); \tag{25} $$

we can scale our three-way data in a fashion analogous to our two-way data. Thus, our noise scaled data is obtained using

$$ {}_{ij}\tilde{\mathbf{F}}_{k} = {}_{ij}\mathbf{F}_{k}\mathbf{\Omega}_{k}^{-1/2}, \tag{26} $$

$$ {}_{ki}\tilde{\tilde{\mathbf{F}}}_{j} = {}_{ki}\tilde{\mathbf{F}}_{j}\mathbf{\Psi}_{j}^{-1/2}, \text{ and} \tag{27} $$

$$ {}_{jk}\tilde{\tilde{\tilde{\mathbf{F}}}}_{i} = {}_{jk}\tilde{\tilde{\mathbf{F}}}_{i}\mathbf{\Phi}_{i}^{-1/2}. \tag{28} $$

After TLD is accomplished utilizing the noise-scaled data, the resulting factors matrices, ${}_{i}\tilde{\mathbf{C}}_{r}$, ${}_{j}\tilde{\mathbf{S}}_{r}$, and ${}_{k}\tilde{\mathbf{T}}_{r}$; are re-scaled to the same domain as our original data, so

$$ {}_{i}\mathbf{C}_{r} = {}_{i}\mathbf{\Phi}_{i}^{1/2}\tilde{\mathbf{C}}_{r}, \tag{29} $$

$$ {}_{j}\mathbf{S}_{r} = {}_{j}\mathbf{\Psi}_{j}^{1/2}\tilde{\mathbf{S}}_{r}, \text{ and} \tag{30} $$

$$ {}_{k}\mathbf{T}_{r} = {}_{k}\mathbf{\Omega}_{k}^{1/2}\tilde{\mathbf{T}}_{r}. \tag{31} $$

Following the same strategy as the unscaled data, we performed a rank estimation for the noise-scaled data. The results of the eigenanalysis are presented in Figure 5.3. We infer a rank three model for these data in at least two of the three modes. The third eigenvalue for the temporal mode is quite close to the level of the noise eigenvalues. Given the previous results and the predominance of rank three estimates, we elected to confer on the data a rank three estimate overall.

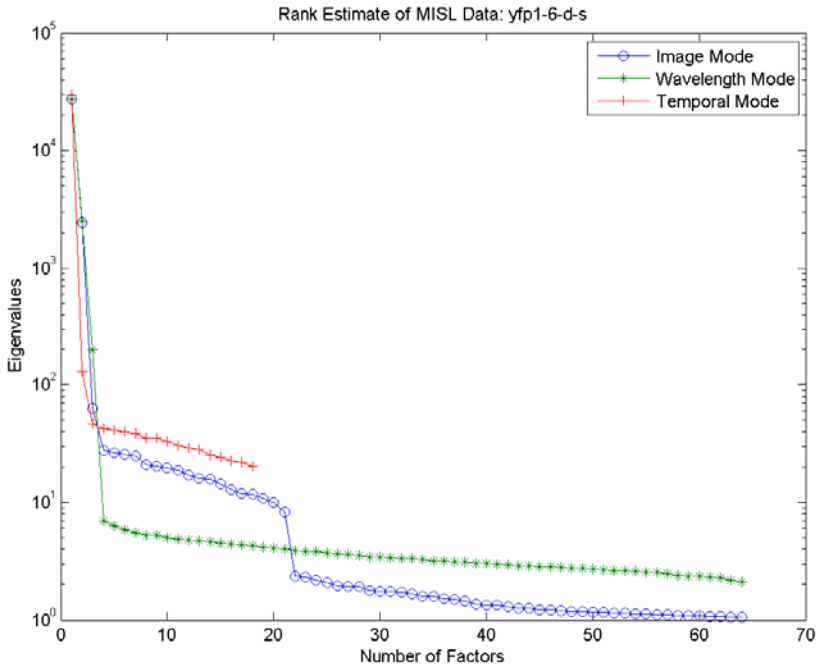

Figure 5.3. Eigenvalues of noise-scaled 3D hyperspectral microscope image array. Blue, green, and red are the image, wavelength and temporal modes, respectively. From these modes, we infer a rank-three array.

As in the first analysis, we employed a rigorous least squares nonnegativity constraint to the first 200 iterations of the TLD to preclude two-factor degeneracy. The results of the rank three analysis are on display in Figure 54. Clearly, we have three spectrally distinct species. They are the dark current, AF and YFP. Their photodecomposition profiles are also easily distinguishable from one-another and appear to follow our experiential models. The images of the compressed data are highly pixilated, however, they show the YFP-marked cell, the AF in a variety of cells and the ubiquitous nature of the dark-current. Unfortunately, our expectation for the dark-current was a uniform random spatial distribution; but it is more correlated with the cell positions than predicted. Analysis of the residuals still showed some structured components in the wavelength and temporal mode, although the image mode appeared completely randomized. By projecting the full 200 $\times$ 200 image data into the space spanned by the TLD resolved spectral and temporal modes; we were able to generate the full presented in Figure 54.

The full-image components have some substantial negative pixels that make the results difficult to analyze. It is difficult to say if these have any physical significance, but they are most likely artifacts of the least squares process. These may be a consequence of lack of fit resulting from the use of compressed images. To improve interpretation of the full data images, we set a threshold for the negative intensity of 10% of the minimum (largest negative) value. These results can be viewed in Figure 54.

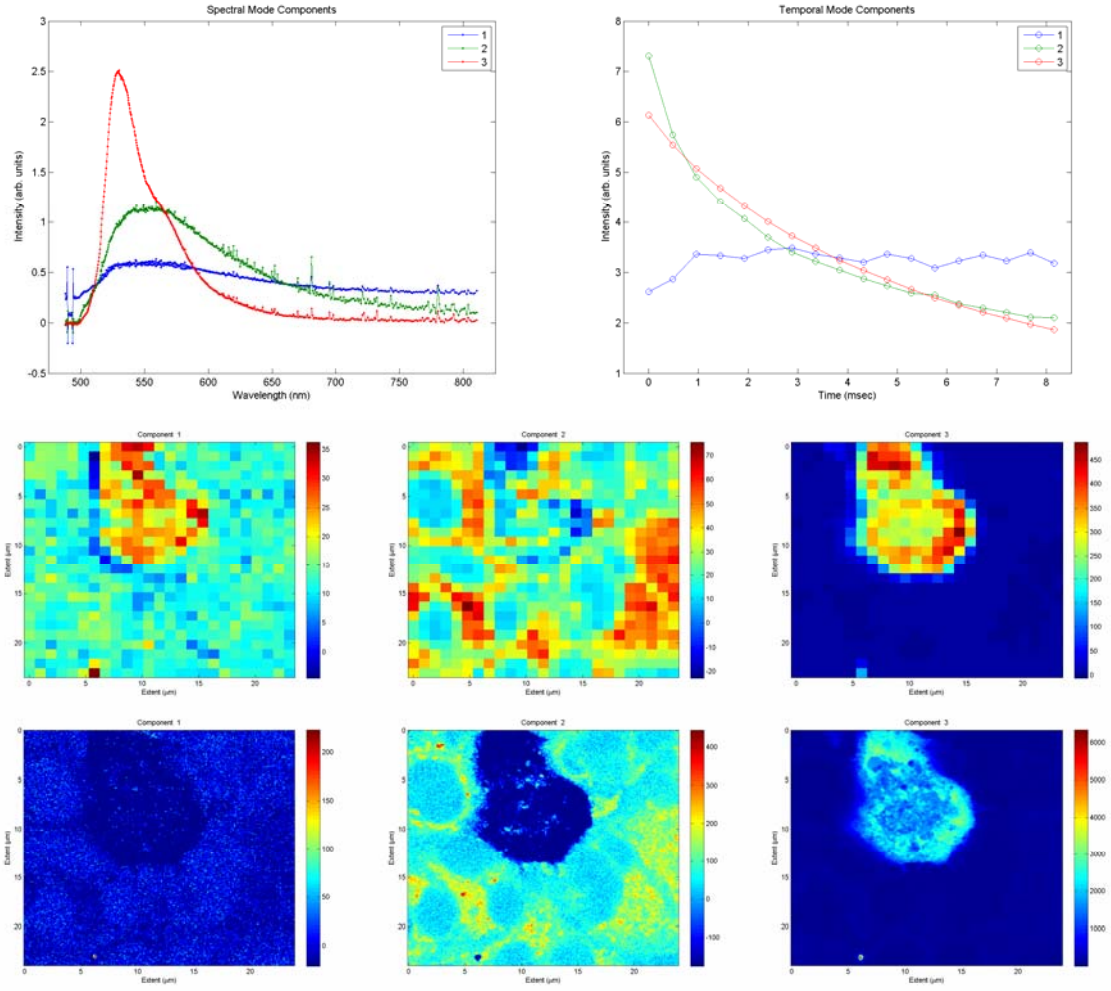

Figure 54. Compressed, noise-scaled, 3D hyperspectral microscope data using three component model TLD. Top L-R: Three component model spectral profiles and temporal profiles. Middle L-R: Compressed image mode derived for each of the three components. Bottom L-R: Full image mode derived for each of the three components. Full images were thresholded at 10% of their maximum negative signal to improve contrast.

Section 5 References

5.1 Sinclair, M. B.; Haaland, D. M.; Timlin, J. A.; Jones, H. D. T. *Applied Optics* **2006**, *45*, 6283.
5.2 Tucker, L. R. *Psychometrika* **1966**, *31*, 279.
5.3 Harshman, R. A.; Lundy, M. E. *Computational Statistics & Data Analysis* **1994**, *18*, 39.
5.4 Bro, R. *Chemometrics and Intelligent Laboratory Systems* **1997**, *38*, 149.
5.5 Kruskal, J. B. Rank, Decomposition, and Uniqueness for 3-way and N-way Arrays. In *Multiway Data Analysis*; Coppi, R., Bolasco, S., Eds.; North-Holland: Amsterdam, 1989; pp 7.
5.6 Mitchell, B. C.; Burdick, D. S. *Journal of Chemometrics* **1994**, *8*, 155.
5.7 Leurgans, S. E.; Ross, R. T. *Statistical Science* **1992**, *7*, 289.
5.8 Tomasi, G.; Bro, R. *Computational Statistics & Data Analysis* **2006**, *50*, 1700.
5.9 Van Loan, C. F. *Journal of Computational and Applied Mathematics* **2000**, *123*, 85.
5.10 Sanchez, E.; Kowalski, B. R. *Journal of Chemometrics* **1990**, *4*, 29.
5.11 Andersson, C. A.; Bro, R. *Chemometrics and Intelligent Laboratory Systems* **1998**, *42*, 93.
5.12 Bro, R. Multi-way Analysis in the Food Industry. Dissertation, University of Amsterdam, 1998.
5.13 MATLAB; 7.2.0.232 (R2006a) ed.; The MathWorks, Inc.: Natick, MA, 2006.
5.14 Wickerhauser, M. V. *Adapted Wavelet Analysis from Theory to Software*; AK Peters, Ltd.: Wellesley, MA, 1994.
5.15 Van Benthem, M. H.; Keenan, M. R. *Journal of Chemometrics* **2004**, *18*, 441.
5.16 Keenan, M. R.; Kotula, P. G. *Applied Surface Science* **2004**, *231/232*, 240.

Conclusions

The design, construction and demonstration of a new hyperspectral confocal fluorescence microscope have been completed during this project. Coupling the hyperspectral image analysis with efficient and rigorous MCR software serves to form a new imaging technology that greatly improves fluorescence imaging capabilities for biological samples. New capabilities include the imaging of multiple spectrally and spatially overlapped fluorophores, significant improvements in quantitative images, and discovery of processes occurring in cells that were not previously known. Already in spin-off projects from this work, we have been able to image multiple fluorescent proteins in live cells along with the cell autofluorescence and/or structural stains for investigating host-pathogen interactions occurring as part of the innate immune system. We have also performed kinetic hyperspectral imaging to quantitatively monitor and localize processes occurring in live cells in response to cytokines. Hyperspectral imaging of antimicrobial peptides (AMPs) and their interactions with bacteria is being conducted to help understand the mechanisms and kinetics of the interaction of the AMPs with the bacteria. Imaging of biofilms on water purification membranes is now helping to understand and reduce the detrimental effects of biofilm formation on the membranes. We are also imaging multiple fluorescent quantum dots in cells to monitor cell signaling processes in live cells. Finally, we are teaming with US industry to perform hyperspectral imaging and analysis of high ethanol producing corn plants in a program to improve the efficiency of ethanol production from corn for biofuels applications.

DISTRIBUTION

	MS0123	Donna Chavez, LDRD Office, 01011*
1	MS0895	Haaland, David M., 08332
2	MS0899	Technical Library, 04536
2	MS9018	Central Technical Files, 08944

Electronic copies to:

Bachand, George D.
Davidson, George S.
Jones, Howland D. T.
Nieman, Linda T. (linda.nieman@gmail.com)
Sasaki, Darryl Y.
Sinclair, Michael B.
Timlin, Jerilyn A.
Van Benthem, Mark H.

*SAND number only